Hidden Markov model tracking of continuous gravitational waves from young supernova remnants

L. Sun,[1,*] A. Melatos,[1,†] S. Suvorova,[2,1] W. Moran,[2] and R. J. Evans[3,1]

[1]*ozGrav, University of Melbourne, Parkville, Victoria 3010, Australia*
[2]*School of Electrical and Computer Engineering, RMIT University, Melbourne, Victoria 3000, Australia*
[3]*Department of Electrical and Electronic Engineering, University of Melbourne,*
Parkville, Victoria 3010, Australia

Searches for persistent gravitational radiation from nonpulsating neutron stars in young supernova remnants are computationally challenging because of rapid stellar braking. We describe a practical, efficient, semicoherent search based on a hidden Markov model tracking scheme, solved by the Viterbi algorithm, combined with a maximum likelihood matched filter, the $\mathcal{F}$ statistic. The scheme is well suited to analyzing data from advanced detectors like the Advanced Laser Interferometer Gravitational Wave Observatory (Advanced LIGO). It can track rapid phase evolution from secular stellar braking and stochastic timing noise torques simultaneously without searching second- and higher-order derivatives of the signal frequency, providing an economical alternative to stack-slide-based semicoherent algorithms. One implementation tracks the signal frequency alone. A second implementation tracks the signal frequency and its first time derivative. It improves the sensitivity by a factor of a few upon the first implementation, but the cost increases by 2 to 3 orders of magnitude.

I. INTRODUCTION

Rotating neutron stars in young supernova remnants (SNRs) are plausible sources of quasi-monochromatic gravitational radiation detectable by ground-based interferometers such as the Laser Interferometer Gravitational Wave Observatory (LIGO) and the Virgo detector [1–3]. The emission is predicted to occur at a frequency proportional to the star's spin frequency $f_\star$. A thermoelastic [4,5] or magnetic [6–8] mass quadrupole emits at $f_\star$ and/or $2f_\star$, an r-mode current quadrupole emits at roughly $4f_\star/3$, perturbed by an equation-of-state correction [9–12], and a current quadrupole produced by nonaxisymmetric circulation in a superfluid pinned to the crust emits at $f_\star$ [13–16]. There are several reasons to devote attention to this source class. First, a young object has spent less time settling down since its birth; slow, diffusive processes like ohmic [17] or thermal [18] relaxation are still in the early stages of erasing nonaxisymmetries inherited at birth [1,3,19]. Second, the rapid spin-down of a differentially rotating young neutron star excites high-Reynolds-number turbulence, which produces a time-varying current quadrupole moment [13,20,21]. Third, young radio pulsars are known to undergo glitches [22–25], which are ascribed to

differential rotation [26–28] or starquakes [29] and can also lead to quadrupole moment variations.

Initial LIGO achieved its design sensitivity over a wide frequency band during Science Run 5 (S5) [30] and exceeded it during Science Run 6 (S6) [2]. Several continuous-wave searches targeting young SNRs have been carried out using Initial LIGO data. A directed, radiometer search for SNR 1987A was conducted in S5, yielding a 90% confidence strain upper limit $h_0^{90\%} = 7 \times 10^{-25}$ for a circularly polarized signal in the most sensitive band, near 160 Hz [31].[1] A semicoherent cross-correlation search for the same target in S5 data improved the upper limit to $h_0^{90\%} = 3.8 \times 10^{-25}$ [33]. A coherent search for Cassiopeia A (Cas A) was conducted on a 12-day stretch of S5 data in the band 100–300 Hz, yielding $h_0^{95\%}$ in the range 0.7–1.2×10^{-24} [34]. The upper limit for Cas A was improved by approximately a factor of 2 by a semicoherent Einstein@Home search in S6. The search was conducted in a broad frequency band 50–1000 Hz, yielding the best $h_0^{90\%} \approx 2.9 \times 10^{-25}$ at 170 Hz [35]. In S6, directed searches were conducted for nine nonpulsating x-ray sources (central compact objects) in SNRs with the maximum likelihood matched filter called the $\mathcal{F}$ statistic. The searches

---

[*]lings2@student.unimelb.edu.au
[†]amelatos@unimelb.edu.au

[1]The radiometer search assumes a circularly polarized signal. The upper limit quoted here converts to $h_0^{90\%} = 1.6 \times 10^{-24}$ for the general case of arbitrary polarization after multiplying by a sky-position-dependent factor ≈ 2.2 [32].

combine multidetector data coherently over 5.3 to 25.3 days, yielding strain upper limits in the range $3.7 \times 10^{-25} \leq h_0^{95\%} \leq 6.4 \times 10^{-25}$ [36]. The foregoing upper limits are slated to improve in the future. The strain noise in the first observation run (O1) of Advanced LIGO is 3–4 times lower than in S6 across the most sensitive band, between 100 Hz and 300 Hz, and $\sim 10^2$ times lower around 50 Hz [37]. The sensitivity is expected to improve roughly twofold relative to O1 after further upgrades [37].

The rapid spin-down of young neutron stars is a serious challenge for searches of the above kind. A large number of matched filters (i.e., templates) is required to track a signal with a rapid evolving phase, when a radio ephemeris is unavailable. For example, the $\mathcal{F}$-statistic search in Ref. [36] is restricted to ≤ 25.3 d in order to keep the number of matched filters manageable. Semicoherent methods have been developed [38–40], based on the stack-slide algorithm [41], to sum the signal power in multiple coherent segments after sliding the segments in the frequency domain to account for the phase evolution of the source. However, stack-slide searches are still computationally challenging, when high-order derivatives of the signal frequency enter the phase model. Intrinsic, stochastic $f_\star$ wandering ("timing noise") also degrades the sensitivity of these searches.

In this paper, we introduce an approach based on a hidden Markov model (HMM) [42] to tackle the above challenge. A HMM tracks signals with time-varying, unobservable parameters by modeling them as hidden states in a Markov chain. The HMM relates the observed data to the hidden states through a likelihood statistic and infers the most probable sequence of hidden states. It incoherently combines the coherent matched filter outputs from data blocks of duration T_{drift} (analogous to T_{span} in Ref. [36]), during which the signal parameters are assumed to remain constant. The sensitivity scales approximately proportional to $(T_{\text{obs}} T_{\text{drift}})^{-1/4}$, where T_{obs} is the whole observation time. The Viterbi algorithm [43] provides a computationally efficient HMM solution. A HMM was applied to search for continuous gravitational radiation from the most luminous low-mass x-ray binary, Scorpius X-1, in O1 data, taking into account the effects of spin wandering caused by the fluctuating accretion torque [44].

The structure of the paper is as follows. In Sec. II, we describe the signal model, introduce the $\mathcal{F}$ statistic, and discuss the search parameter ranges. In Sec. III, we formulate the HMM tracking problem with one hidden state variable, describe how to choose T_{drift}, and discuss the impact of timing noise. In Sec. IV, we conduct Monte Carlo simulations in Gaussian noise, present search examples, and estimate the sensitivity. In Sec. V, we introduce an alternative HMM formulation with two hidden state variables, and present abridged simulation examples. In Sec. VI, we discuss the trade-off between computing cost and sensitivity. We also discuss the special case of young objects, whose current spin frequencies are close to the

value at birth. A summary of the conclusions is provided in Sec. VII.

II. COHERENT MATCHED FILTER

In this section we start by describing the signal model in Sec. II A. We then review the maximum likelihood matched filter corresponding to the signal model, called the $\mathcal{F}$ statistic, in Sec. II B, and discuss the signal phase parameter ranges in Sec. II C.

A. Signal model

We consider a continuous gravitational wave signal from a rotating neutron star modeled as a biaxial rotor. The Doppler modulation of the observed signal frequency due to the motion of the Earth with respect to the solar system barycenter (SSB) is taken into consideration. The signal phase observed at the detector is then given by [45]

$$\Phi(t) = 2\pi \sum_{k=0}^{s} \frac{f_0^{(k)} t^{k+1}}{(k+1)!} + \frac{2\pi}{c} \hat{n} \cdot \vec{r}(t) \sum_{k=0}^{s} \frac{f_0^{(k)} t^k}{k!}, \quad (1)$$

where $f_0^{(k)}$ is the kth time derivative of the signal frequency at $t = 0$, $\hat{n}$ is the unit vector pointing from the SSB to the neutron star, and $\vec{r}(t)$ is the position vector of the detector relative to the SSB.

The signal can be written in the form

$$h(t) = \mathcal{A}^\mu h_\mu(t), \quad (2)$$

where $\mathcal{A}^\mu$ denotes the amplitudes associated with the four linearly independent components[2]

$$h_1(t) = a(t) \cos \Phi(t), \quad (3)$$

$$h_2(t) = b(t) \cos \Phi(t), \quad (4)$$

$$h_3(t) = a(t) \sin \Phi(t), \quad (5)$$

$$h_4(t) = b(t) \sin \Phi(t), \quad (6)$$

$a(t)$ and $b(t)$ are the antenna-pattern functions defined by Eqs. (12) and (13) in Ref. [45], and $\Phi(t)$ is the signal phase given by (1). In (2), $\mathcal{A}^\mu$ depends on the star's inclination, wave polarization, initial phase at $t = 0$, and strain amplitude h_0.

---

[2]Here we assume a perpendicular rotor emitting at $2f_\star$ only for simplicity. A nonperpendicular rotor also emits at $f_\star$, and hence eight components are involved. A full description of the signal model can be found in Ref. [45]. The emission spectrum of a triaxial rotor contains additional lines [8,46].

B. $\mathcal{F}$ statistic

The time-domain data collected by a detector takes the form

$$x(t) = \mathcal{A}^\mu h_\mu(t) + n(t), \tag{7}$$

where $n(t)$ stands for stationary, additive noise. The $\mathcal{F}$ statistic maximizes the likelihood of detecting a signal in data $x(t)$ with respect to $\mathcal{A}^\mu$ [45]. We define a scalar product $(\cdot|\cdot)$ as a sum over single-detector inner products,

$$(x|y) = \sum_X (x^X|y^X) \tag{8}$$

$$= \sum_X 4\Re \int_0^\infty df \frac{\tilde{x}^X(f)\tilde{y}^{X*}(f)}{S_h^X(f)}, \tag{9}$$

where X indexes the detector, $S_h^X(f)$ is the single-sided power spectral density (PSD) of detector X, the tilde denotes a Fourier transform, and $\Re$ returns the real part of a complex number [47]. The $\mathcal{F}$ statistic is expressed in the form

$$\mathcal{F} = \frac{1}{2} x_\mu \mathcal{M}^{\mu\nu} x_\nu, \tag{10}$$

where we write $x_\mu = (x|h_\mu)$, and $\mathcal{M}^{\mu\nu}$ denotes the matrix inverse of $\mathcal{M}_{\mu\nu} = (h_\mu|h_\nu)$.

Assuming the noise $n(t)$ is Gaussian, the random variable $2\mathcal{F}$ follows a noncentral chi-squared distribution with 4 degrees of freedom, whose probability density function (PDF) is

$$p(2\mathcal{F}) = \chi^2(2\mathcal{F}; 4, \rho_0^2), \tag{11}$$

with noncentrality parameter [45]

$$\rho_0^2 = \mathcal{A}^\mu \mathcal{M}_{\mu\nu} \mathcal{A}^\nu. \tag{12}$$

Without a signal, the PDF of $2\mathcal{F}$ centralizes to $p(2\mathcal{F}) = \chi^2(2\mathcal{F}; 4, 0)$. Given a signal in Gaussian noise and assuming the same single-sided PSD, $S_h(f)$, in all detectors, the optimal signal-to-noise ratio equals ρ_0, given by [45,48]

$$\rho_0^2 = \frac{K h_0^2 T_{\mathrm{drift}}}{S_h(f)}, \tag{13}$$

where the constant K depends on the sky location, orientation of the source and the number of detectors, and h_0 denotes the characteristic gravitational-wave strain.

We leverage the existing, fully tested $\mathcal{F}$-statistic software infrastructure in the LSC Algorithm Library Applications (LALApps)[3] to compute $\mathcal{F}$ as a function of frequency and its time derivatives over an interval of length T_{drift} [49]. The

software operates on the raw data collected by LIGO in the form of short Fourier transforms (SFTs), usually with length $T_{\mathrm{SFT}} = 30$ min for each SFT. It provides options to search up to the third time derivative of frequency, $\dddot{f}_0$. The implementations described in Secs. III and V use the options to search over f_0 and $(f_0, \dot{f}_0)$, respectively.

C. Search parameter ranges

The ranges of $\dot{f}_0$ and $\ddot{f}_0$ to be considered in defining the parameters of the search can be reexpressed in terms of the range of braking index $n = f_0\ddot{f}_0/\dot{f}_0^2$ and the spin-down age of the source τ, given by [34,36]

$$-\frac{f_0}{(n_{\min}-1)\tau} \le \dot{f}_0 \le -\frac{f_0}{(n_{\max}-1)\tau}, \tag{14}$$

and

$$\frac{n_{\min}\dot{f}_0^2}{f_0} \le \ddot{f}_0 \le \frac{n_{\max}\dot{f}_0^2}{f_0}. \tag{15}$$

Radio timing observations yield $1.4 \le n \le 3$ for all pulsars, where $\ddot{f}_0$ can be measured reliably by absolute pulse numbering [9,50] (cf. [51]). Gravitational radiation in the mass and current quadrupole channels corresponds to $n = 5$ and $n = 7$, respectively. In this quick study, we assume $2 \le n \le 7$. Strictly speaking, the ranges obtained from (14) and (15) are wider than needed. In a real search, one should ideally calculate the $\dot{f}_0$ and $\ddot{f}_0$ ranges for each fixed $2 \le n \le 7$ and choose the widest $\dot{f}_0$ and $\ddot{f}_0$ ranges. Equations (14) and (15) are valid, provided that $f_0(t)$ during the observation is much smaller than f_0 at birth, $f_{0\mathrm{birth}}$. The regime $f_0(t) \sim f_{0\mathrm{birth}}$ is considered in Sec. VI B.

III. HMM TRACKING OF f_0

We begin this section by reviewing briefly the use of HMM tracking in gravitational wave searches (Sec. III A). We formulate the tracker as a one-dimensional HMM with a single hidden variable f_0 (Sec. III B), discuss the coherent drift time scale T_{drift} (Sec. III C), and illustrate that the method can track secular spin-down and stochastic timing noise simultaneously (Sec. III D). A full description of HMMs can be found in Ref. [48]. The Viterbi algorithm used for solving the HMM is described in Appendix A.

A. HMM formulation

A Markov chain is a stochastic process transitioning between discrete states at discrete times $\{t_0, ..., t_{N_T}\}$. A HMM is an automaton, in which the state variable $q(t) \in \{q_1, ..., q_{N_Q}\}$ is hidden (unobservable), and the measurement variable $o(t) \in \{o_1, ..., o_{N_O}\}$ is observable. The

---

hidden state at time t_{n+1} only depends on the state at time t_n with transition probability

$$A_{q_j q_i} = P[q(t_{n+1}) = q_j | q(t_n) = q_i]. \qquad (16)$$

The hidden state q_i is observed in state o_j with emission probability

$$L_{o_j q_i} = P[o(t_n) = o_j | q(t_n) = q_i]. \qquad (17)$$

Given the prior defined by

$$\Pi_{q_i} = P[q(t_0) = q_i], \qquad (18)$$

the probability that the hidden state path $Q = \{q(t_0), \ldots, q(t_{N_T})\}$ gives rise to the observed sequence $O = \{o(t_0), \ldots, o(t_{N_T})\}$ via a Markov chain equals

$$P(Q|O) = L_{o(t_{N_T}) q(t_{N_T})} A_{q(t_{N_T}) q(t_{N_T-1})} \cdots L_{o(t_1) q(t_1)}$$
$$\times A_{q(t_1) q(t_0)} \Pi_{q(t_0)}. \qquad (19)$$

The most probable path maximizing $P(Q|O)$, viz.

$$Q^*(O) = \arg\max P(Q|O), \qquad (20)$$

gives the best estimate of $q(t)$ over the total observation, where $\arg\max(\cdots)$ returns the argument that maximizes the function $(\cdots)$.

B. Transition and emission probabilities

We consider the one-dimensional hidden state variable $q(t) = f_0(t)$. The discrete hidden states are mapped one-to-one to the frequency bins in the output of a frequency-domain estimator $\mathcal{F}(f_0)$ computed over an interval of length T_{drift}, with bin size Δf_0 selected using the metric described in Appendix B. For simplicity here, we take $\Delta f_0 = 1/(2T_{\text{drift}})$, with mismatch $m \leq 0.2$. The mismatch m is defined as the fractional reduction of $\mathcal{F}$-statistic power caused by discrete parameter sampling (see Appendix B). We choose T_{drift} as described in Sec. III C to satisfy

$$\left| \int_t^{t+T_{\text{drift}}} dt' \dot{f}_0(t') \right| < \Delta f_0 \qquad (21)$$

for $0 < t < T_{\text{obs}}$.

In this section, we first consider the situation where the time scale of timing noise, which causes f_0 to walk randomly, is much longer than the spin-down time scale. Hence the impact of timing noise is negligible compared to secular spin-down. Modifications needed to tackle stronger timing noise are discussed in Sec. III D. If we substitute the maximum $|\dot{f}_0|$ from (14), denoted by $|\dot{f}_0|_{\text{max}}$, into (21) and

assume that $\dot{f}_0$ is uniformly distributed in the range from zero to $|\dot{f}_0|_{\text{max}}$,[4] Eq. (16) simplifies to

$$A_{q_{i-1} q_i} = A_{q_i q_i} = \frac{1}{2}, \qquad (22)$$

with all other entries being zero. By the definition of the frequency domain estimator, the emission probability is given by [45,48,49]

$$L_{o(t) q_i} = P[o(t) | f_{0i} \leq f_0(t) \leq f_{0i} + \Delta f_0] \qquad (23)$$

$$\propto \exp[\mathcal{F}(f_{0i})], \qquad (24)$$

during the interval $[t, t + T_{\text{drift}}]$, where f_{0i} is the value of f_0 in the ith f_0 bin. Since we have no independent knowledge of f_0, we choose a uniform prior, viz.

$$\Pi_{q_i} = N_Q^{-1}. \qquad (25)$$

C. Drift time scale

Given $\dot{f}_0$, we choose T_{drift} according to

$$|\dot{f}_0| T_{\text{drift}} = \Delta f_0 = \frac{1}{2T_{\text{drift}}}, \qquad (26)$$

to satisfy (21). Hence $T_{\text{drift}} = (2|\dot{f}_0|)^{-1/2}$ depends solely on the spin-down rate of the source. To illustrate how T_{drift} is determined by τ, we calculate $\dot{f}_0$ and hence T_{drift} by assuming purely electromagnetic spin-down [$\dot{f}_0(t) \propto B_0^2 f_0(t)^n$, $n = 3$] as an example, where B_0 is the birth magnetic field strength; see Appendix C for a detailed derivation. Figure 1 displays contours of T_{drift} as a function of the gravitational-wave signal frequency today, $f_{0\text{today}}$, and the ratio $f_{0\text{today}}/f_{0\text{birth}}$, where $f_{0\text{birth}}$ is the signal frequency at the birth of the star. The contours in the upper left panel (e.g., SNR 1987A; $\tau = 0.03$ kyr) show $T_{\text{drift}} \lesssim 5$ h for most of the plot. By contrast, the contours in the upper right panel (e.g., Cas A; $\tau = 0.34$ kyr) satisfy $T_{\text{drift}} > 10$ h over $\approx 1/3$ area of the plot. The T_{drift} values estimated for older objects with $\tau = 0.6$ kyr and 1 kyr are plotted in the lower panels. All panels show that T_{drift} decreases significantly for $f_{0\text{today}}/f_{0\text{birth}} \lesssim 0.8$ and $f_{0\text{today}} \gtrsim 100$ Hz.

---

[4]According to Eq. (14), we have $|\dot{f}_0|_{\text{max}} = 6|\dot{f}_0|_{\text{min}}$, where $|\dot{f}_0|_{\text{min}}$ is the minimum $|\dot{f}_0|$ from (14). In practice, however, we normally search $|\dot{f}_0|$ values more than an order of magnitude smaller than $|\dot{f}_0|_{\text{max}}$. Hence the search range of $\dot{f}_0$ is dominated by $|\dot{f}_0|_{\text{max}}$, and we approximate the search range to be $0 \leq |\dot{f}_0| \leq |\dot{f}_0|_{\text{max}}$.
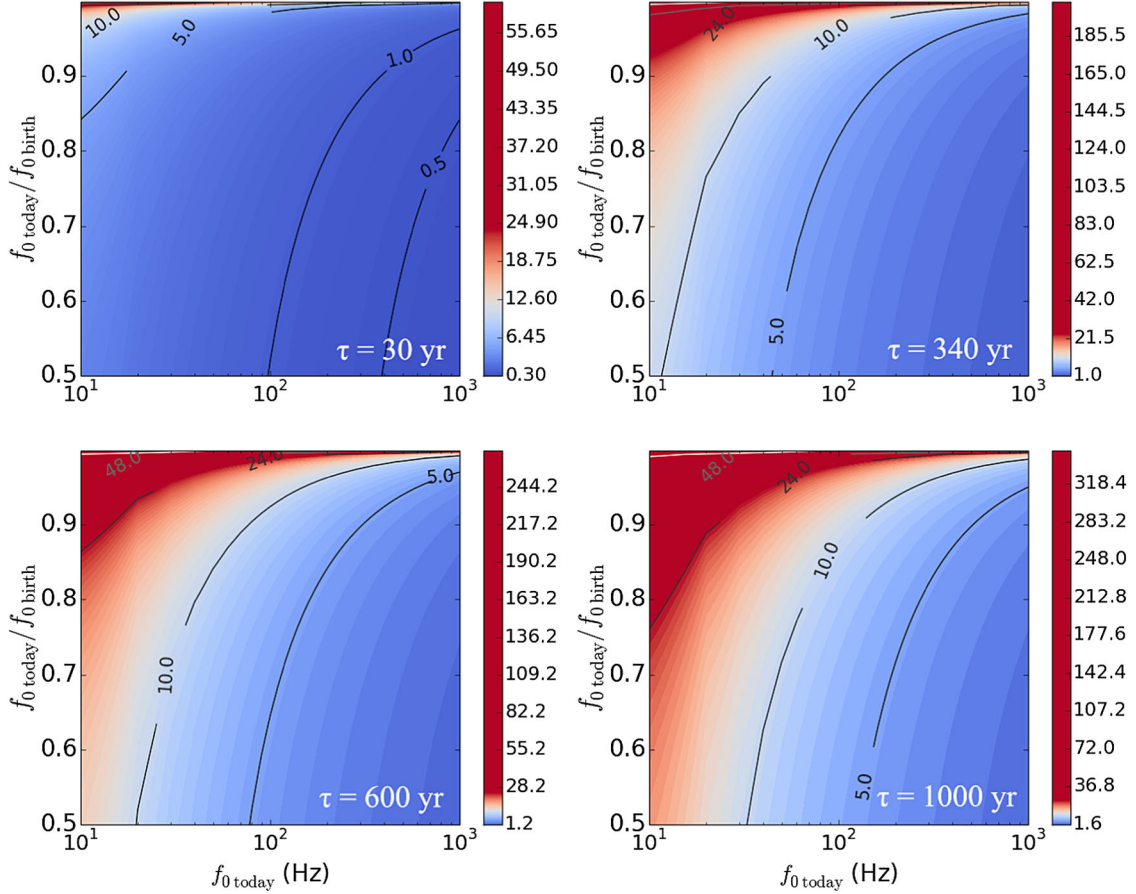
FIG. 1. Contours of T_{drift} (in hours) for targets with $\tau = 0.03$ kyr (top left), 0.34 kyr (top right), 0.6 kyr (bottom left), and 1 kyr (bottom right) as a function of the gravitational-wave signal frequency today $f_{0\mathrm{today}}$ and the ratio $f_{0\mathrm{today}}/f_{0\mathrm{birth}}$, where $f_{0\mathrm{birth}}$ is the signal frequency at the birth of the star, assuming pure electromagnetic spin-down ($\dot{f}_0 \propto B_0^2 f_0^n$, $n = 3$).

Figure 1 is plotted for $n = 3$. In practice, the range of $\dot{f}_0$ is given by Eq. (14) for $2 \leq n \leq 7$. We substitute $|\dot{f}_0|_{\mathrm{max}}$ into (26) to satisfy (21) for all $\dot{f}_0$ and obtain

$$T_{\mathrm{drift}} = (2|\dot{f}_0|_{\mathrm{max}})^{-1/2}. \qquad (27)$$

Hence for any given source with spin-down age τ, we can always choose a coherent duration T_{drift} and divide the data into $N_T = T_{\mathrm{obs}}/T_{\mathrm{drift}}$ coherent segments, without searching the $(\dot{f}_0, \ddot{f}_0, \ldots)$ parameter space.

D. Timing noise

Stochastic spin wandering (often termed timing noise) is a widespread phenomenon in isolated neutron stars pulsating at radio and x-ray wavelengths [52–54]. The autocorrelation time scale ranges from days to years [55,56]. The phenomenon can result from magnetospheric changes [57], superfluid dynamics in the stellar interior [56,58–60], spin microjumps [61,62], and fluctuations in the spin-down torque [63–65].

In the absence of a measured ephemeris, a HMM can track the evolution of $f_0(t)$ caused by both secular spin-down and stochastic timing noise [48]. We approximate the timing noise by an unbiased random walk, in which $f_0(t)$ moves by at most one bin up or down during the timing-noise time scale T'_{drift}. The transition probability matrix for timing noise only is

$$A'_{q_{i-1}q_i} = A'_{q_i q_i} = A'_{q_{i+1}q_i} = \frac{1}{3}. \qquad (28)$$

For $T'_{\mathrm{drift}} \gg T_{\mathrm{drift}}$, we can neglect timing noise, as discussed in previous sections. For $T'_{\mathrm{drift}} \ll T_{\mathrm{drift}}$, we can neglect secular spin-down, set $A_{q_j q_i} = A'_{q_j q_i}$, and divide the data into $N_T = T_{\mathrm{obs}}/T'_{\mathrm{drift}}$ coherent segments. For $T'_{\mathrm{drift}} \approx T_{\mathrm{drift}}$, we choose $\min(T'_{\mathrm{drift}}, T_{\mathrm{drift}})$ as the drift time scale and adjust the transition probabilities to take into consideration both timing noise and spin-down.

IV. SIMULATIONS AND SENSITIVITY

In this section, we first introduce the Viterbi score and the associated, score-based detection threshold in

Sec. IV A. We demonstrate the performance of f_0 tracking for three different scenarios using synthetic data: (1) an older object with weak timing noise (Sec. IV B); (2) an older object with strong timing noise (Sec. IV C); and (3) a very young object (Sec. IV D). Simulations are conducted in an artificially restricted, 1-Hz subband to save time. The signals are injected at a fixed sky position, and $S_h(f)$ is set to Advanced LIGO's design sensitivity [66]. We show the results in detail with a set of injections into Gaussian noise for each of the three scenarios, where the polarization and inclination angles and initial phase are arbitrarily chosen and fixed. Monte Carlo simulations are conducted to generate the receiver operator characteristic (ROC) curves (Sec. IV E).

A. Viterbi score and threshold

The Viterbi score S is defined such that the log likelihood of the optimal Viterbi path equals the mean log likelihood of all paths plus S standard deviations at t_{N_T}, viz.

$$S = \frac{\ln \delta_{q^*}(t_{N_T}) - \mu_{\ln \delta}(t_{N_T})}{\sigma_{\ln \delta}(t_{N_T})} \quad (29)$$

with

$$\mu_{\ln \delta}(t_{N_T}) = N_Q^{-1} \sum_{i=1}^{N_Q} \ln \delta_{q_i}(t_{N_T}) \quad (30)$$

and

$$\sigma_{\ln \delta}(t_{N_T})^2 = N_Q^{-1} \sum_{i=1}^{N_Q} [\ln \delta_{q_i}(t_{N_T}) - \mu_{\ln \delta}(t_{N_T})]^2, \quad (31)$$

where $\delta_{q_i}(t_{N_T})$ denotes the maximum probability of the path ending in state q_i ($1 \leq i \leq N_Q$) at step N_T (see Appendix A), and $\delta_{q^*}(t_{N_T})$ is the likelihood of the optimal Viterbi path, i.e., $P[Q^*(O)|O]$. In a real search, we normally divide the full frequency band into multiple 1-Hz subbands to allow parallelized computing. In each 1-Hz subband, we consider the candidate for follow-up and further scrutiny, if S exceeds a threshold $S_{\rm th}$ set by the desired false alarm and false dismissal probabilities. The value of $S_{\rm th}$ varies with N_T, N_Q, and the entries in $A_{q_j q_i}$. Systematic Monte Carlo simulations are always required in practice to calculate $S_{\rm th}$ for each HMM implementation.

For the three scenarios in Secs. IV B–IV D, $S_{\rm th}$ is determined as follows. Searches are conducted on data sets containing pure Gaussian noise in 1-Hz subbands. For a given false alarm probability P_a in a 1-Hz subband, the value of S yielding a fraction P_a of positive detections is $S_{\rm th}$. The false alarm probability in a search over band B is given by $P_{a,\rm total} = 1 - (1 - P_a)^B$. We set $P_a = 1\%$ and generate 10^3 noise realizations for each scenario. Searches

for the first two scenarios are based on the same N_T and N_Q, and hence they both yield $S_{\rm th} = 6.7$. The mean and standard deviation of S in the 10^3 realizations are $\mu_S = 5.5$ and $\sigma_S = 0.4$. In the last scenario, we have $S_{\rm th} = 0.8$, with $\mu_S = 0.63$ and $\sigma_S = 0.06$. Because $\sigma_{\ln \delta}(t_{N_T})$ increases as N_T gets larger, yielding lower S normalized by $\sigma_{\ln \delta}(t_{N_T})$ in (29), it is as expected that the $S_{\rm th}$ is much lower in the last scenario ($N_T = 2000$) than the first two scenarios ($N_T = 40$).

B. $\tau \gtrsim 5$ kyr, $T'_{\rm drift} \gg T_{\rm drift}$

In the first group of tests, we consider a relatively older target with low timing noise, e.g., $\tau \gtrsim 5$ kyr and $T'_{\rm drift} \gg T_{\rm drift}$. Four sets of synthetic data, containing injected signals with $h_0/10^{-26} = 10$, 5, 3, and 2, are generated for $T_{\rm obs} = 83.3$ d at two detectors (the LIGO Hanford and Livingston observatories) using MAKEFAKEDATA version 4 from LALApps. Detailed injection parameters are shown in Table I. The searches are conducted using the search parameters in Table II and $A_{q_j q_i}$ in (22). The detection is deemed successful for $S > S_{\rm th} = 6.7$. The results in Table III show that signals with $h_0 \geq 3 \times 10^{-26}$ are detected. We calculate the root-mean-square error (RMSE) ε_{f_0} in f_0 between the optimal Viterbi path and the injected signal (in Hz and in units of Δf_0). All successful detections yield $\varepsilon_{f_0} < \Delta f_0$. The errors are introduced mostly because the HMM takes discrete values of f_0 (i.e., Δf_0 is the smallest step size), while the injected signal $f_0(t)$ can take any value within a bin.

TABLE I. Injection parameters used to create the synthetic data analyzed in Secs. IV B and IV C.

Parameter	Symbol	Value
Right ascension	α	23 h 23 m 26.0 s
Declination	δ	58°48′0.0″
Polarization angle	ψ	4.94278 rad
Inclination angle	$\cos \iota$	0.718742
Initial phase	ϕ_0	2.43037 rad
PSD	$S_h(f)^{1/2}$	4×10^{-24} Hz$^{-1/2}$
Frequency	$f_{0\rm inj}$	151.23456789 Hz
First derivative of $f_{0\rm inj}$	$\dot{f}_{0\rm inj}$	-1.0×10^{-11} Hz s^{-1}
Second derivative of $f_{0\rm inj}$	$\ddot{f}_{0\rm inj}$	2.0×10^{-24} Hz s^{-2}

TABLE II. Search parameters for the synthetic signals with injection parameters quoted in Table I.

Parameter	Value	Unit
f_0	151–152	Hz
$T_{\rm drift}$	50	h
Δf_0	2.78×10^{-6}	Hz
$T_{\rm obs}$	83.3	d
N_T	40	

TABLE III. Results of f_0 tracking for synthetic signals with the injection parameters in Table I, $T_{obs} = 83.3$ d, $T_{drift} = 50$ h, and characteristic wave strain h_0. The RMSE ε_{f_0} between the optimal Viterbi path and the injected $f_0(t)$ is quoted in Hz and in units of $\Delta f_0 = 2.78 \times 10^{-6}$ Hz. The third column quotes the Viterbi score S.

h_0 (10^{-26})	Detect?	S	ε_{f_0} [Hz]	$\varepsilon_{f_0}/\Delta f_0$
10.0	✓	90.9	1.07×10^{-6}	0.39
5.0	✓	32.0	1.29×10^{-6}	0.46
3.0	✓	10.6	1.64×10^{-6}	0.59
2.0	✗	5.5	0.46	1.6×10^5

Figure 2 presents the tracking results corresponding to Table III. Figures 2(a)–2(c) show that the optimal Viterbi paths match the injected $f_0(t)$ closely, with $\varepsilon_{f_0} = 0.39\Delta f_0$, $0.46\Delta f_0$, and $0.59\Delta f_0$, respectively. Figure 2(d) shows that

the signal is not tracked successfully. The detectability drops rapidly from $h_0 = 3 \times 10^{-26}$ to $h_0 = 2 \times 10^{-26}$, as expected near the detection limit (see detailed explanation in Sec. III B of Ref. [48]).

C. $\tau \gtrsim 5$ kyr, $T'_{drift} \approx T_{drift}$

In the second group of tests, we show that the HMM can track secular spin-down and timing noise simultaneously for synthetic signals injected in Gaussian noise. As an example, we assume the time scale of the unbiased random walk is the same as the spin-down time scale, i.e., $T'_{drift} = T_{drift} = 50$ h. The modified transition probability matrix is the product of (22) and (28), given by

$$2A_{q_{i-2}q_i} = A_{q_{i-1}q_i} = A_{q_iq_i} = 2A_{q_{i+1}q_i} = \frac{1}{3}, \quad (32)$$

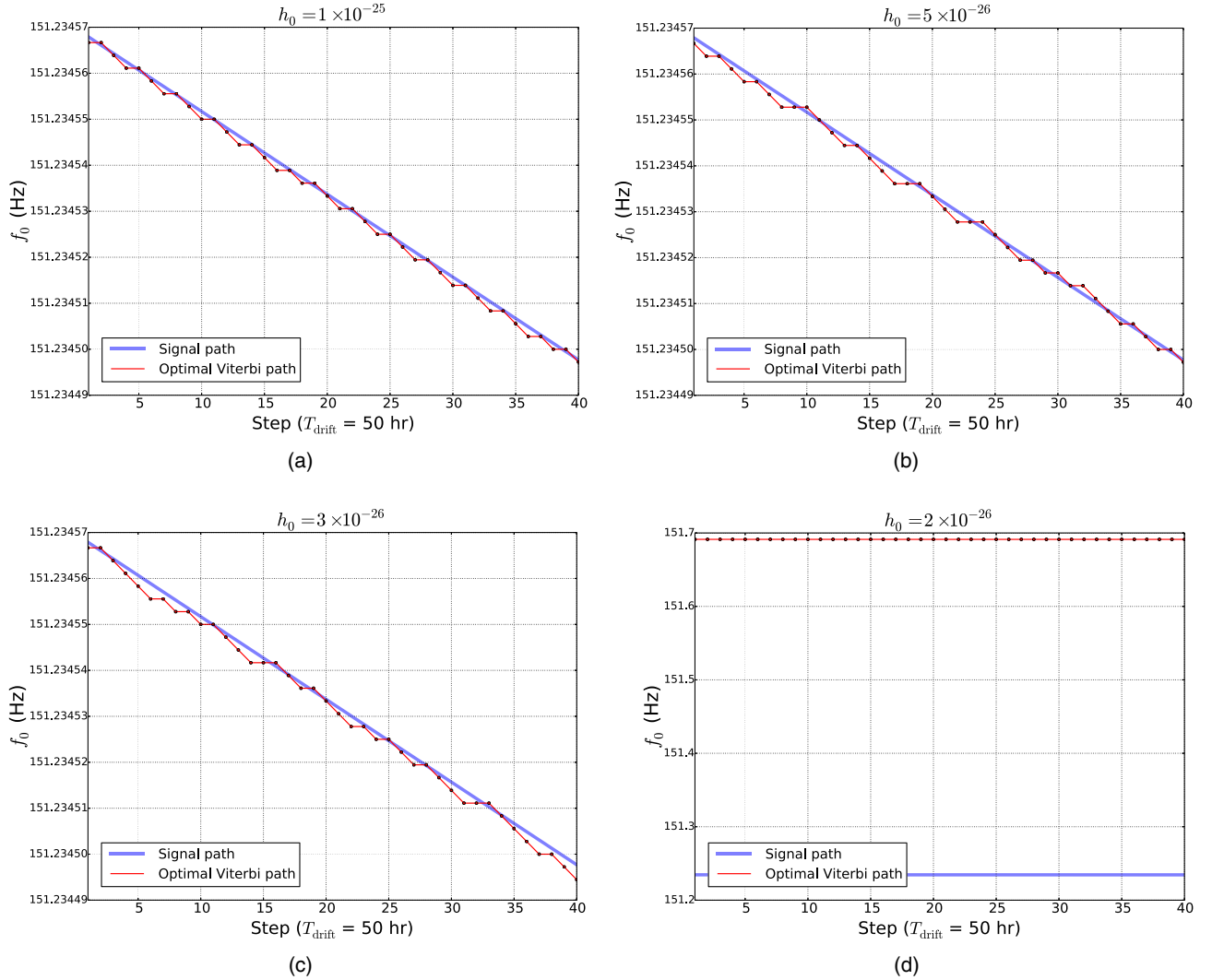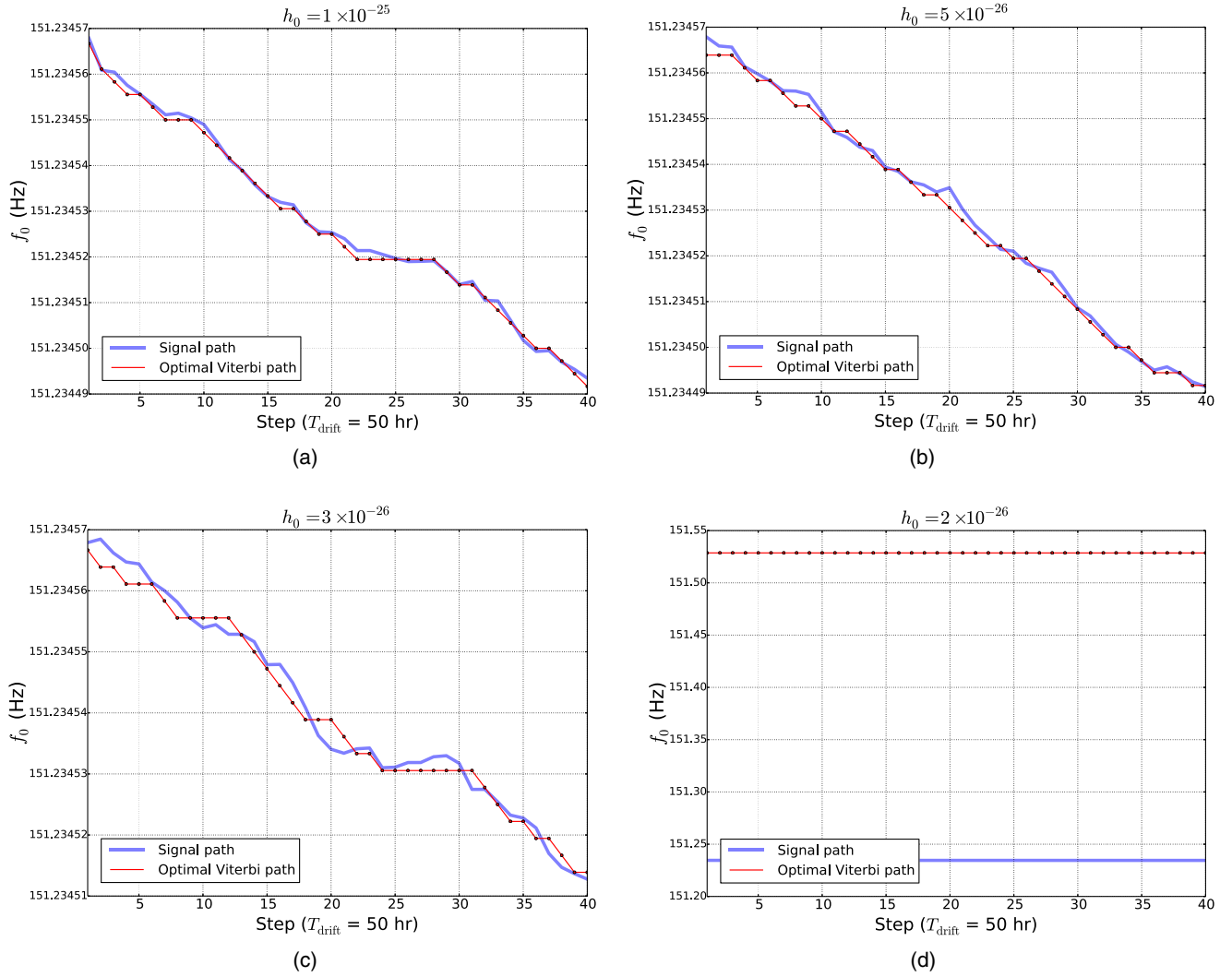with all other terms being zero.

FIG. 2. Injected $f_0(t)$ (blue curve) and optimal Viterbi path (red curve) for the injected signals in Table III. Panels (a)–(d) display paths for $h_0/10^{-26} = 10, 5, 3, 2$, respectively. Good matches are obtained in (a)–(c), with $\varepsilon_{f_0} = 0.39\Delta f_0$, $0.46\Delta f_0$, and $0.59\Delta f_0$, respectively. In (d), the signal is not detected; the spin-down of $f_0(t)$ is too slow to be seen in the plot ($\varepsilon_{f_0} \gg \dot{f}_0 T_{obs} = 7 \times 10^{-5}$ Hz). The horizontal axes are in units of HMM steps with $T_{drift} = 50$ h for each step ($N_T = 40$).

FIG. 3.   Injected $f_0(t)$ (blue curve) and optimal Viterbi path (red curve) for the injected signals in Table IV. Panels (a)–(d) display paths for $h_0/10^{-26} = 10, 5, 3, 2$, respectively. Good matches are obtained in (a)–(c), with $\varepsilon_{f_0} = 0.38\Delta f_0, 0.59\Delta f_0$, and $0.77\Delta f_0$, respectively. In (d), the signal is not detected; the spin-down of $f_0(t)$ is too slow to be seen in the plot ($\varepsilon_{f_0} \gg \dot{f}_0 T_{\mathrm{obs}} \sim 7 \times 10^{-5}$ Hz). The horizontal axes are in units of HMM steps with $T_{\mathrm{drift}} = 50$ h for each step ($N_T = 40$).

Four data sets with signal strains $h_0/10^{-26} = 10, 5, 3$, and 2 are generated for $T_{\mathrm{obs}} = 83.3$ d at two detectors. We use the same injection parameters in Table I at $t = 0$. In addition to the spin-down, $f_0(t)$ wanders randomly by at most $\pm\Delta f_0$ over time scale T_{drift}. The data sets are searched using the parameters in Table II and $A_{q_j q_i}$ in (32). The results are shown in Table IV. The detection is deemed successful for $S > S_{\mathrm{th}} = 6.7$. All successful detections yield $\varepsilon_{f_0} < \Delta f_0$.

Figure 3 presents the tracking results for signals with $h_0/10^{-26} = 10, 5, 3, 2$ in Table IV. The optimal Viterbi paths in Figs. 3(a)–3(c) match the injected paths closely, indicating successful detections. The RMSE ε_{f_0} increases from $0.38\Delta f_0$ to $0.77\Delta f_0$, when h_0 decreases from 1×10^{-25} to 3×10^{-26}. Figure 3(d) shows that the optimal Viterbi path does not match the injected $f_0(t)$ for $h_0 = 2 \times 10^{-26}$; i.e., the injected signal is not detected.

Given the signal-to-noise ratio, T_{drift} and N_T, the sensitivity of the search remains the same for $T'_{\mathrm{drift}} \gg T_{\mathrm{drift}}$ (Sec. IV B) and $T'_{\mathrm{drift}} = T_{\mathrm{drift}}$ (Sec. IV C).

TABLE IV.   Results of f_0 tracking for synthetic spin-wandering signals with the injection parameters in Table I, $T_{\mathrm{obs}} = 83.3$ d, $T_{\mathrm{drift}} = 50$ h, and characteristic wave strain h_0. The RMSE ε_{f_0} between the optimal Viterbi path and the injected $f_0(t)$ is quoted in Hz and in units of $\Delta f_0 = 2.78 \times 10^{-6}$ Hz. The third column quotes the Viterbi score S.

h_0 (10^{-26})	Detect?	S	ε_{f_0} [Hz]	$\varepsilon_{f_0}/\Delta f_0$
10.0	✓	92.5	1.06×10^{-6}	0.38
5.0	✓	28.4	1.63×10^{-6}	0.59
3.0	✓	7.2	2.14×10^{-6}	0.77
2.0	×	5.1	0.29	1.1×10^5

TABLE V. Spin-down-related injection parameters used to create the synthetic data analyzed in Sec. IV D.

Parameter	Symbol	Value
First derivative of $f_{0\mathrm{inj}}$	$\dot{f}_{0\mathrm{inj}}$	-3.0×10^{-8} Hz s^{-1}
Second derivative of $f_{0\mathrm{inj}}$	$\ddot{f}_{0\mathrm{inj}}$	3.0×10^{-17} Hz s^{-2}
Third derivative of $f_{0\mathrm{inj}}$	$\dddot{f}_{0\mathrm{inj}}$	-3.0×10^{-26} Hz s^{-3}

D. $\tau \lesssim 0.03$ kyr, $T'_{\mathrm{drift}} \gg T_{\mathrm{drift}}$

In the third group of tests, we consider a very young object with $\tau \lesssim 0.03$ kyr, e.g., SNR 1987A. In stack-slide-based searches for such young sources, typically four or more frequency derivatives must be searched in order to accurately track the rapid phase evolution.

We inject four signals with $h_0/10^{-26} = 15$, 13, 11, 10 and high spin-down rates as quoted in Table V. Other injection parameters remain the same as those in Table I. We choose $T_{\mathrm{drift}} = 1$ h to satisfy Eq. (21). In this case, we always have $T'_{\mathrm{drift}} \gg T_{\mathrm{drift}}$ and hence use $A_{q_j q_i}$ in (22). The search parameters and results are presented in Tables VI and VII, respectively. In this group, the detection is deemed successful for $S > S_{\mathrm{th}} = 0.8$ given $P_a = 1\%$. The successful detections yield $\varepsilon_{f_0} < 2\Delta f_0 = 2.8 \times 10^{-4}$ Hz. We tolerate ε_{f_0} slightly larger than Δf_0 because T_{drift} is relatively short.

Figure 4 shows the tracking results corresponding to Table VII. Figures 4(a)–4(c) show that the optimal Viterbi paths match the injected $f_0(t)$ closely. The discrepancy between the optimal Viterbi path and the injected $f_0(t)$ can

TABLE VI. Search parameters for the synthetic signals with injection parameters quoted in Tables I and V.

Parameter	Value	Unit
f_0	151–152	Hz
T_{drift}	1	h
Δf_0	1.39×10^{-4}	Hz
T_{obs}	83.3	d
N_T	2000	

TABLE VII. Results of f_0 tracking for synthetic signals with the injection parameters in Tables I and V, $T_{\mathrm{obs}} = 83.3$ d, $T_{\mathrm{drift}} = 1$ h, and characteristic wave strain h_0. The RMSE ε_{f_0} between the optimal Viterbi path and the injected $f_0(t)$ is quoted in Hz and in units of $\Delta f_0 = 1.39 \times 10^{-4}$ Hz. The third column quotes the Viterbi score S.

h_0 (10^{-26})	Detect?	S	ε_{f_0} [Hz]	$\varepsilon_{f_0}/\Delta f_0$
15.0	✓	3.0	1.77×10^{-4}	1.3
13.0	✓	2.1	2.50×10^{-4}	1.8
11.0	✓	0.9	2.47×10^{-4}	1.8
10.0	✗	0.5	0.02	151.8

hardly be seen, because $\varepsilon_{f_0} \sim 10^{-4}$ Hz is much smaller than the total change in f_0 over T_{obs} (≈ 0.2 Hz). Figure 4(d) shows that the signal is not detected for $h_0 = 10 \times 10^{-26}$, with $\varepsilon_{f_0} = 151.8\Delta f_0 \gg \Delta f_0$.

E. ROC curve and sensitivity

The detection threshold S_{th} is set by P_a. The probability that an injected signal yields $S < S_{\mathrm{th}}$ is the false dismissal probability, denoted by P_d. We quantify the performance of the HMM in terms of its ROC curve, plotting the detection probability $1 - P_d$ against the false alarm probability P_a for various signal strengths. The signal-to-noise ratio for a biaxial rotor scales approximately in proportion to h_0^{eff}, given by [45,67]

$$h_0^{\mathrm{eff}} = h_0 2^{-1/2} \{[(1 + \cos^2\iota)/2]^2 + \cos^2\iota\}^{1/2}, \quad (33)$$

so we quote h_0^{eff} instead of h_0 as the signal strength. The simulations are conducted in an artificially restricted, 1-Hz subband, at a fixed sky location, with both polarization angle ψ and initial phase Φ_0 randomly chosen with a uniform distribution within the range $[0, 2\pi]$ rad.

The ROC curves are essentially indistinguishable for the two scenarios in Secs. IV B and IV C, because HMM tracking is insensitive to the exact choice of $A_{q_j q_i}$ [42,43]. Figure 5 shows the ROC curves for these two scenarios with four values of h_0^{eff}, ranging from 1.8×10^{-26} to 2.5×10^{-26}. For $P_a = 1\%$, we have 85% and 99% confidence to detect a signal with $h_0^{\mathrm{eff}} = 2.2 \times 10^{-26}$ and 2.5×10^{-26}, respectively, read off the top two curves in Fig. 5. The 95% confidence sensitivity on effective strain is $h_0^{\mathrm{eff},95\%} \approx 2.4 \times 10^{-26}$ ($T_{\mathrm{obs}} = 83.3$ d).

Figure 6 shows the ROC curves for the searches in Sec. IV D with four h_0^{eff} values, ranging from 7.5×10^{-26} to 9.0×10^{-26}. The properties of the curves are similar to Fig. 5. However, the overall sensitivity degrades by a factor of ≈ 3.5, with $h_0^{\mathrm{eff},95\%} \approx 8.5 \times 10^{-26}$ ($T_{\mathrm{obs}} = 83.3$ d).

V. HMM TRACKING OF f_0 AND $\dot{f}_0$

In Secs. III and IV, we show that one-dimensional HMM tracking can be applied to search for any young objects, but the sensitivity degrades when the spin-down rate is too high, e.g., $|\dot{f}_0| \gtrsim 10^{-8}$ Hz s^{-1} and $T_{\mathrm{drift}} \lesssim$ a few hours. In this section, we describe a more costly alternative to f_0 tracking, which allows relatively longer T_{drift} when the spin-down rate is high. We formulate the tracker as a two-dimensional HMM with hidden state $(f_0, \dot{f}_0)$ in Sec. V A and present simulation examples in Sec. V B.

A. Transition and emission probabilities

In this implementation, we define a two-dimensional hidden state variable $q(t) = [f_0(t), \dot{f}_0(t)]$ and track f_0 and
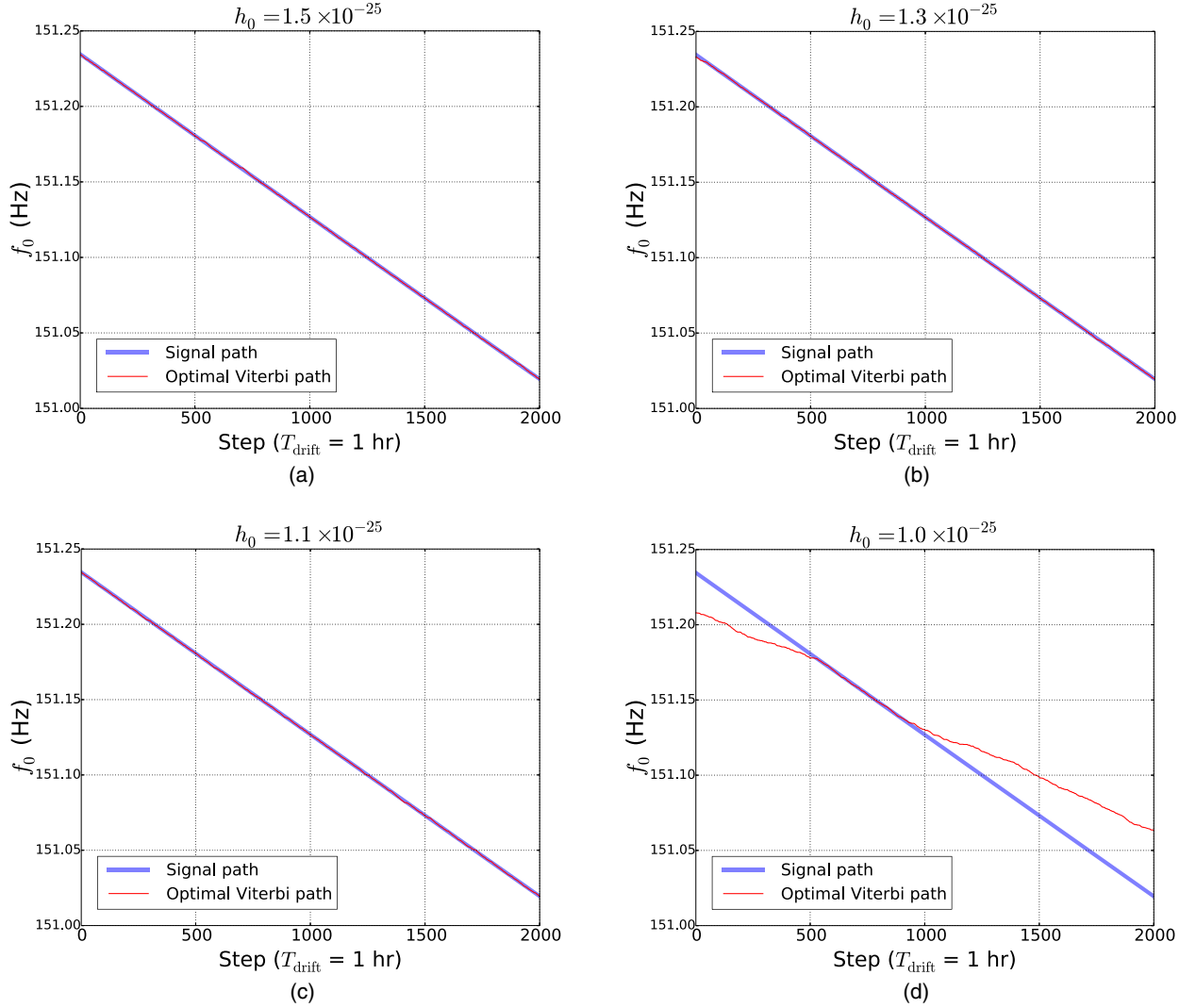
FIG. 4. Injected $f_0(t)$ (blue curve) and optimal Viterbi path (red curve) for the injected signals in Table VII. Panels (a)–(d) display paths for $h_0/10^{-26} = 15, 13, 11, 10$, respectively. Good matches are obtained in (a)–(c), with $\varepsilon_{f_0} < 2\Delta f_0$. In panel (d), the signal is not detected. The horizontal axes are in units of HMM steps with $T_{\text{drift}} = 1$ h for each step ($N_T = 2000$).

$\dot{f}_0$ jointly. The state variable can take $N_Q = N_{f_0} N_{\dot{f}_0}$ possible discrete values $q_{ij} \in \{q_{11}, \ldots, q_{N_{f_0} N_{\dot{f}_0}}\}$, where i and j index f_0 and $\dot{f}_0$ bins, respectively, and N_{f_0} and $N_{\dot{f}_0}$ are the total number of f_0 and $\dot{f}_0$ bins, respectively.

The discrete hidden states are mapped one-to-one to the two-dimensional array of bins in the output of the estimator $\mathcal{F}(f_0, \dot{f}_0)$ computed over T_{drift}.[5] The f_0 and $\dot{f}_0$ bin sizes Δf_0 and $\Delta \dot{f}_0$ are selected using a phase metric described in Appendix B. Assuming that the spin-down evolution of a neutron star is smooth (i.e., no glitches) and that $\ddot{f}_0(t)$ is bounded, we can always choose an intermediate time

scale T_{drift} for a particular astrophysical source, $T_{\text{SFT}} < T_{\text{drift}} < T_{\text{obs}}$, to satisfy

$$\left| \int_t^{t+T_{\text{drift}}} dt' \ddot{f}_0(t') \right| < \Delta \dot{f}_0 \qquad (34)$$

for $0 < t < T_{\text{obs}}$. We calculate $f_0(t_{n+1})$ from the estimated $f_0(t_n)$ and $\dot{f}_0(t_n)$ according to[6]

$$f_0(t_{n+1}) = f_0(t_n) + \dot{f}_0(t_n) T_{\text{drift}}. \qquad (35)$$

---

[5]The $\mathcal{F}$ statistic is computed as a function of $f_0(t)$ and $\dot{f}_0(t)$ at a given reference time. We normally choose the start time t_n of the interval as the reference time.

[6]Alternatively, if we track $f_0(t)$ and $\dot{f}_0(t)$ independently, another constraint on T_{drift} is imposed by Δf_0, given by (21). In other words, we cannot use longer T_{drift} than that in the f_0 tracking. Hence we do not track f_0 and $\dot{f}_0$ independently and choose T_{drift} to satisfy (34) only.
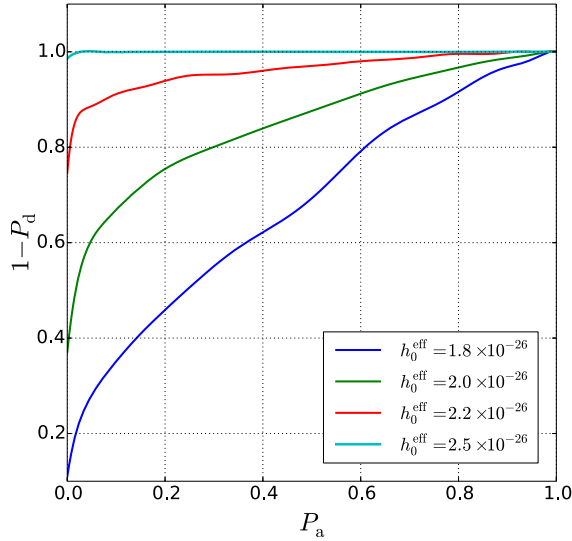
FIG. 5.   ROC curves for the searches described in Secs. IV B and IV C (curves indistinguishable to the eye). The four curves (from top to bottom) correspond to the four representative wave strains $h_0^{\text{eff}}/10^{-26} = 2.5, 2.2, 2.0$, and 1.8. The horizontal and vertical axes indicate the false alarm probability P_a and detection probability $1 - P_d$, respectively. Each curve is based on 500 realizations. Parameters: $T_{\text{drift}} = 50$ h, $N_T = 40$, $S_h(f)^{1/2} = 4 \times 10^{-24}$ Hz$^{-1/2}$.
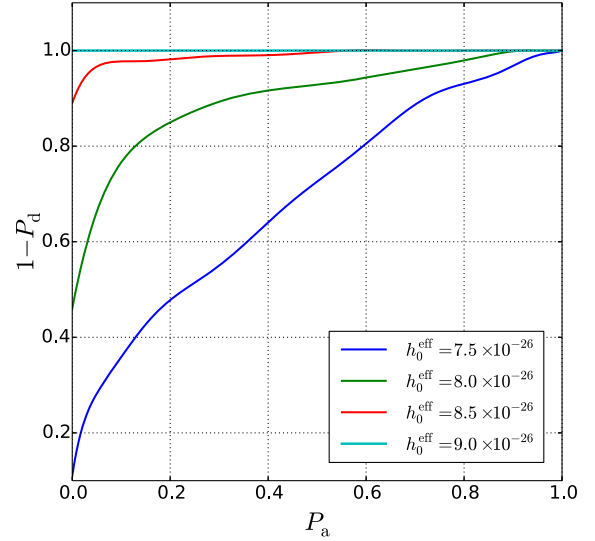
FIG. 6.   ROC curves for the searches described in Sec. IV D. The four curves (from top to bottom) correspond to the four representative wave strains $h_0^{\text{eff}}/10^{-26} = 9.0, 8.5, 8.0$, and 7.5. The horizontal and vertical axes indicate the false alarm probability P_a and detection probability $1 - P_d$, respectively. Each curve is based on 200 realizations. Parameters: $T_{\text{drift}} = 1$ h, $N_T = 2000$, $S_h(f)^{1/2} = 4 \times 10^{-24}$ Hz$^{-1/2}$.

If we update $f_0(t_{n+1})$ according to (35), the transition probability matrix becomes

$$A_{q_{i-\Delta i,j+1} q_{ij}} = A_{q_{i-\Delta i,j} q_{ij}}$$
$$= \{2[\Delta i_{\max}(j) - \Delta i_{\min}(j) + 1]\}^{-1}, \quad (36)$$

with all other terms being zero. In (36), Δi takes integer values $\Delta i_{\min}(j) \leq \Delta i \leq \Delta i_{\max}(j)$ with

$$\Delta i_{\min}(j) = \text{floor}(|\dot{f}_{0 j+1}| T_{\text{drift}}/\Delta f_0), \quad (37)$$

$$\Delta i_{\max}(j) = \text{ceil}(|\dot{f}_{0 j}| T_{\text{drift}}/\Delta f_0), \quad (38)$$

where floor(x) denotes the largest integer smaller than or equal to x, ceil(x) denotes the smallest integer larger than or equal to x, and $\dot{f}_{0j}$ is the value of $\dot{f}_0$ in the jth $\dot{f}_0$ bin. The detailed derivation of (36) is given in Appendix D.

The emission probability is given by

$$L_{o(t)q_{ij}} = P[o(t)|f_{0i} \leq f_0(t) \leq f_{0i} + \Delta f_0,$$
$$\dot{f}_{0j} \leq \dot{f}_0(t) \leq \dot{f}_{0j} + \Delta \dot{f}_0] \quad (39)$$

$$\propto \exp[\mathcal{F}(f_{0i}, \dot{f}_{0j})]. \quad (40)$$

We choose a uniform prior in both f_0 and $\dot{f}_0$, viz.

$$\Pi_{q_{ij}} = N_Q^{-1}. \quad (41)$$

B. Abridged mock search

In this section we demonstrate the $(f_0, \dot{f}_0)$ HMM tracker using synthetic data. To make a fair comparison with the f_0 tracker, we conduct an abridged version of a mock search for the rapidly spinning down signal simulated in Sec. IV D, with the same injection parameters as in Tables I and V. We choose $T_{\text{drift}} = 50$ h ($N_T = 40$) to satisfy (34) and use the search parameters in Table VIII. The $\mathcal{F}$ statistic is computed over a 1-Hz frequency band as a function of f_0 and $\dot{f}_0$ for each segment. For demonstration purposes, only five values of $\dot{f}_0$ are searched in a range containing the injected $\dot{f}_0$ to save time; i.e., the phase metric is not computed.

The results are presented in Table IX. Compared to the performance displayed in Table VII using f_0 tracking, the

TABLE VIII.   Search parameters for the synthetic signals with injection parameters quoted in Tables I and V.

Parameter	Value	Unit
f_0	151–152	Hz
$-\dot{f}_0$	2.98×10^{-8}–3.02×10^{-8}	Hz s^{-1}
T_{drift}	50	h
Δf_0	2.78×10^{-6}	Hz
$\Delta \dot{f}_0$	1×10^{-10}	Hz s^{-1}
T_{obs}	83.3	d
N_T	40	

TABLE IX.   Results of $(f_0, \dot{f}_0)$ tracking for injected signals with the parameters in Tables I and V, $T_{\text{obs}} = 83.3$ d, $T_{\text{drift}} = 50$ h, and wave strain h_0. The RMSE ε_{f_0} between the frequency of the optimal Viterbi path and the injected $f_0(t)$ is quoted in Hz and in units of $\Delta f_0 = 2.78 \times 10^{-6}$ Hz. The RMSE $\varepsilon_{\dot{f}_0}$ between the frequency derivative of the optimal Viterbi path and the injected $\dot{f}_0(t)$ is quoted in Hz s^{-1} and in units of $\Delta \dot{f}_0 = 1 \times 10^{-10}$ Hz s^{-1}. The third column quotes the Viterbi score S.

h_0 (10^{-26})	Detect?	S	ε_{f_0} [Hz]	$\varepsilon_{f_0}/\Delta f_0$	$\varepsilon_{\dot{f}_0}$ [Hz s^{-1}]	$\varepsilon_{\dot{f}_0}/\Delta \dot{f}_0$
8.0	✓	9.0	2.89×10^{-6}	1.0	2.97×10^{-11}	0.30
5.0	✓	2.9	6.45×10^{-6}	2.3	3.56×10^{-11}	0.36
4.0	✓	2.0	1.80×10^{-5}	6.5	2.85×10^{-11}	0.29
3.0	✗	1.2	0.45	1.6×10^5	1.659×10^{-10}	1.59

$(f_0, \dot{f}_0)$ tracking can detect a signal about 3 times weaker. We calculate the RMSE ε_{f_0} in f_0 between the optimal Viterbi path and the injected signal (in Hz and in units of Δf_0). We do the same for the RMSE $\varepsilon_{\dot{f}_0}$ in $\dot{f}_0$ (in Hz s^{-1} and in units of $\Delta \dot{f}_0$). In a real search, we consider candidates for follow-up and further scrutiny, if S exceeds a threshold S_{th} set by the desired false alarm and false dismissal probabilities, as shown in Sec. IV. The value of S_{th} depends strongly on N_Q and hence the two-dimensional $(f_0, \dot{f}_0)$ parameter space. Systematic Monte Carlo simulations are required in practice to calculate S_{th} for each HMM implementation, an exercise lying outside the scope of this paper. Instead, in this section, we adopt the following rule of thumb: the injected signal is deemed to be detected if we obtain $\varepsilon_{\dot{f}_0} < 0.5\Delta \dot{f}_0$ and $\varepsilon_{f_0} < 10\Delta f_0$. The errors are introduced mostly because HMM takes discrete values of f_0 and $\dot{f}_0$, while the injected signal $f_0(t)$ and $\dot{f}_0(t)$ can be any value within a bin. Since we calculate $f_0(t_{n+1})$ from the estimated $f_0(t_n)$ and $\dot{f}_0(t_n)$, ε_{f_0} accumulates to a few Δf_0 after N_T steps, introduced by $\varepsilon_{\dot{f}_0}$.

Figure 7 displays the optimal Viterbi paths (red curves) and the true paths $f_0(t)$ and $\dot{f}_0(t)$ (blue curves) for the two weakest injections (a) $h_0 = 4 \times 10^{-26}$ and (b) $h_0 = 3 \times 10^{-26}$. The left and right panels show f_0 and $\dot{f}_0$, respectively. In Fig. 7(a), the optimal Viterbi paths agree with $f_0(t)$ and $\dot{f}_0(t)$ closely. In the right panel, it is shown that the estimated $\dot{f}_0$ fluctuates within one bin around the injected $\dot{f}_0(t)$. The fluctuations around f_0 cannot be seen clearly in the left panel, because $\varepsilon_{f_0} = 1.80 \times 10^{-5}$ Hz is much smaller than the total change of f_0 over T_{obs} (≈ 0.2 Hz). In contrast, Fig. 7(b) shows that the optimal Viterbi paths do not match the injected $f_0(t)$ and $\dot{f}_0(t)$; i.e., the injected signal is not detected.

VI. DISCUSSION

A. Cost-sensitivity trade-off

In this section, we start by comparing the HMM tracking method to existing stack-slide-based semicoherent methods and then discuss the cost-sensitivity trade-off between $(f_0, \dot{f}_0)$ tracking and f_0 tracking. Analytic approximations for

the computing cost and sensitivity are described briefly in Appendixes B and E.

HMM tracking incoherently combines the $\mathcal{F}$-statistic outputs from $N_T = T_{\text{obs}}/T_{\text{drift}}$ blocks of data. The computing cost is composed of two parts: (1) calculating the coherent $\mathcal{F}$ statistic (i.e., $L_{o_j q_i}$) for all N_T segments; and (2) recursively maximizing $P(Q|O)$, i.e., solving the HMM. Assuming we use data from two interferometers and search up to the maximum frequency $f_{0\text{max}}$, the computing costs of calculating $\mathcal{F}(f_0)$ and $\mathcal{F}(f_0, \dot{f}_0)$ over one block of coherent segment T_{drift} are given by

$$\mathcal{T}_{f_0} = 0.46 \text{ d} \left(\frac{f_{0\text{max}}}{0.6 \text{ kHz}}\right) \left(\frac{T_{\text{drift}}}{10 \text{ d}}\right)^2 \left(\frac{1}{N_{\text{core}}}\right), \quad (42)$$

and

$$\mathcal{T}_{f_0, \dot{f}_0} = 0.36 \text{ d} \left(\frac{f_{0\text{max}}}{0.6 \text{ kHz}}\right)^2 \left(\frac{0.3 \text{ kyr}}{\tau}\right) \left(\frac{T_{\text{drift}}}{10 \text{ d}}\right)^4 \left(\frac{10^3}{N_{\text{core}}}\right), \quad (43)$$

respectively, where N_{core} is the number of cores running in parallel (see details in Appendix B). The Viterbi algorithm computes $Q^*(O)$ via $(N_T + 1)N_Q \ln N_Q$ operations [48]. For example, in a 1-Hz subband with $N_Q = 2 \times 10^6$ and $N_T = 36$, it takes $\lesssim 30$ s to compute $Q^*(O)$ but $\gtrsim 1$ h to compute N_T blocks of the $\mathcal{F}$ statistic. Hence the total computing cost is dominated by the cost of computing N_T blocks of the $\mathcal{F}$ statistic, scaling as $\mathcal{T}_{f_0} \propto N_T f_{0\text{max}} T_{\text{drift}}^2$ for f_0 tracking, and $\mathcal{T}_{f_0, \dot{f}_0} \propto N_T f_{0\text{max}}^2 \tau^{-1} T_{\text{drift}}^4$ for $(f_0, \dot{f}_0)$ tracking.

Compared to a fully coherent $\mathcal{F}$-statistic search, the cost saving conferred by the HMM tracker is similar to other $\mathcal{F}$-statistic-based semicoherent methods, when only f_0 or $(f_0, \dot{f}_0)$ needs to be searched. Theoretically, the sensitivity of the HMM tracker is also comparable to other $\mathcal{F}$-statistic-based semicoherent searches. Hence the HMM tracker performs on par with other semicoherent methods, as long as the spin-down rate is moderate, except that it is more robust against timing noise, as demonstrated in Sec. IV C.
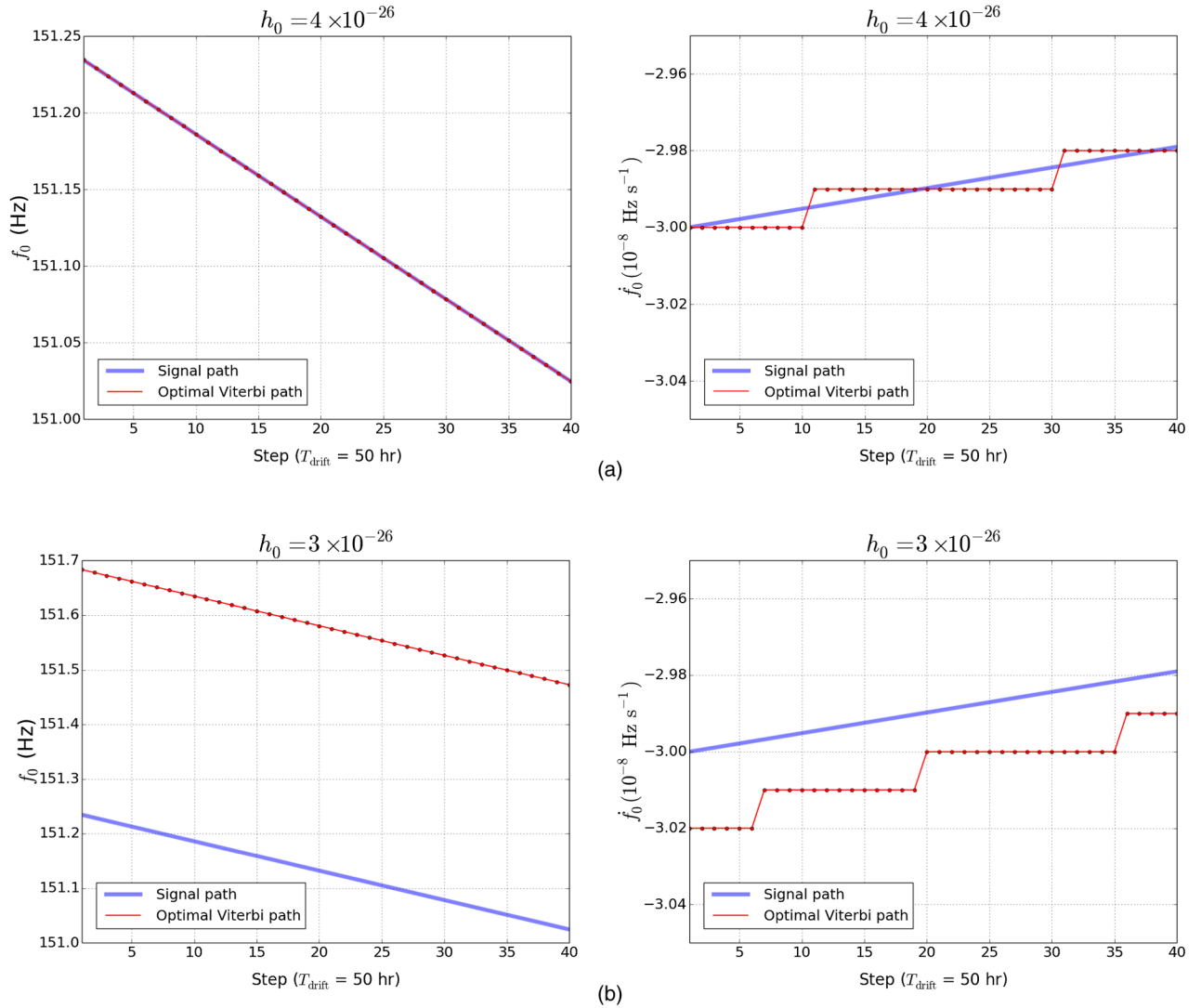
FIG. 7. Injected $f_0(t)$ and $\dot{f}_0(t)$ (blue curves) and optimal Viterbi paths (red curves) for the last two injected signals in Table IX with (a) $h_0 = 4 \times 10^{-26}$ and (b) $h_0 = 3 \times 10^{-26}$. The top left and top right panels show good matches for both f_0 and $\dot{f}_0$, respectively. The red curve in the left panel fluctuates around the blue curve with $\varepsilon_{f_0} = 1.80 \times 10^{-5}$ Hz, which is too small to be seen in the plot ($\varepsilon_{f_0} \ll \dot{f}_0 T_{\mathrm{obs}} \approx 0.2$ Hz). In the lower two panels, the injected signal is not detected. The horizontal axes are in units of HMM steps with $T_{\mathrm{drift}} = 50$ h for each step ($N_T = 40$).

When higher-order derivatives of the frequency are required to be searched for very young objects (e.g., $\tau \lesssim 0.03$ kyr), e.g., in a stack-slide search, the cost of computing the $\mathcal{F}$ statistic grows geometrically as T_{drift} increases. Figure 8 shows the cost of calculating the $\mathcal{F}$-statistic over one block of duration T_{drift} for a target with $\tau = 0.03$ kyr up to $f_{0\mathrm{max}} = 600$ Hz. The three curves, from bottom to top, represent calculating $\mathcal{F}(f_0)$, $\mathcal{F}(f_0, \dot{f}_0)$, and $\mathcal{F}(f_0, \dot{f}_0, \ddot{f}_0)$, respectively. For example, it requires $\sim 10^3$ core-day to compute $\mathcal{F}(f_0, \dot{f}_0, \ddot{f}_0)$ for a single block of duration $T_{\mathrm{drift}} = 4$ d. When $\dddot{f}_0$ needs to be considered, the cost of calculating $\mathcal{F}(f_0, \dot{f}_0, \ddot{f}_0, \dddot{f}_0)$ becomes prohibitive even for $T_{\mathrm{drift}} < 1$ d. Under these circumstances, the HMM tracker comes into its own; it allows an efficient search for

rapidly evolving signals without searching high-order frequency derivatives.

Given fixed T_{obs}, one can tune T_{drift} to trade off sensitivity against computing cost for a particular target. Table X shows the theoretical scalings of sensitivity and cost as a function of T_{drift} for the two HMM implementations described in Secs. III and V. In reality, the scalings vary with many factors, including N_T, P_a, P_d, and the noise statistics, as discussed in detail in Refs. [68,69]. In this paper, we include the theoretical scalings to allow quick order-of-magnitude comparisons, but we emphasize that they are not a substitute for Monte Carlo simulations. The sensitivities of f_0 tracking and $(f_0, \dot{f}_0)$ tracking scale the same way with T_{drift}. An $(f_0, \dot{f}_0)$ search allows longer T_{drift}
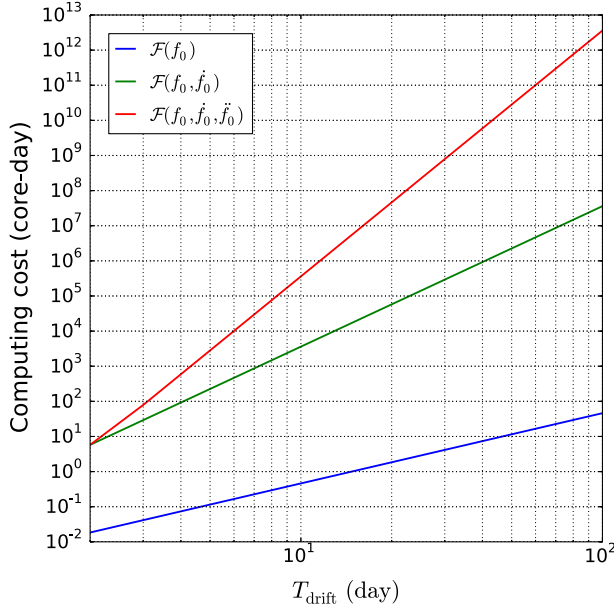
FIG. 8.   Computing cost (in core-days) of a coherent $\mathcal{F}$-statistic search as a function of T_{drift} (in days). The three curves (from bottom to top) represent searching f_0 only, $(f_0, \dot{f}_0)$, and $(f_0, \dot{f}_0, \ddot{f}_0)$, respectively. Parameters: $f_{0\text{max}} = 600$ Hz, $\tau = 0.03$ kyr.

and hence in practice is always more sensitive than an f_0 search. However, an f_0 search is always faster.

Figure 9 plots the ratio $\mathcal{T}_{f_0, \dot{f}_0}/\mathcal{T}_{f_0}$ as a function of τ. The curves, from bottom to top, represent achieving 10%–50% better sensitivity by switching from f_0 tracking to $(f_0, \dot{f}_0)$ tracking. We can always achieve better sensitivity using $(f_0, \dot{f}_0)$ tracking compared to f_0 tracking. However, $\mathcal{T}_{f_0, \dot{f}_0}/\mathcal{T}_{f_0}$ is approximately proportional to τ and increases exponentially with the percentage of sensitivity improvement.

B. Spin-down of young objects with age $\lesssim f_{0\text{birth}}/\dot{f}_{0\text{birth}}$

The true age of a young neutron star may be significantly less than its characteristic spin-down time scale at birth, $f_{0\text{birth}}/[(n-1)\dot{f}_{0\text{birth}}]$, depending on its ellipticity and magnetization. To investigate this scenario, we approximate the braking law with a power law in the usual way, viz. $\dot{f}_0(t) = -\eta f_0(t)^n$, with $\eta \propto B_0^2$ and $2 \lesssim n < 3$ if the torque is electromagnetically dominated, and $\eta \propto \epsilon^2$ and

TABLE X.   Theoretical scalings of sensitivity and computing cost with drift time scale T_{drift} for f_0 tracking (Sec. III) and $(f_0, \dot{f}_0)$ tracking (Sec. V).

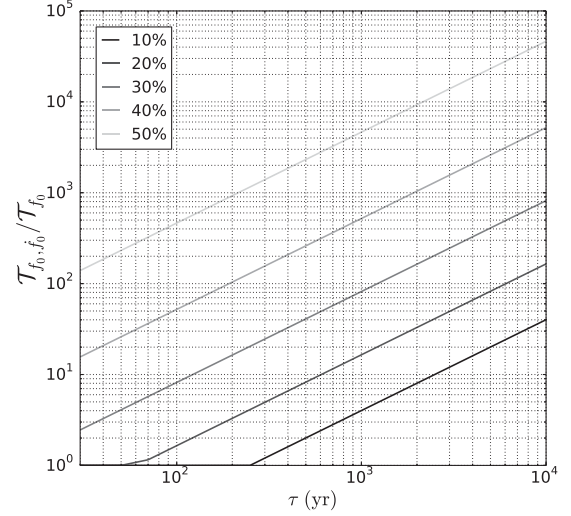| Tracking	Sensitivity	Cost
f_0	$T_{\text{drift}}^{-1/4}$	T_{drift}
f_0 and $\dot{f}_0$	$T_{\text{drift}}^{-1/4}$	T_{drift}^3

FIG. 9.   Ratio of the $(f_0, \dot{f}_0)$ tracking cost $\mathcal{T}_{f_0, \dot{f}_0}$ divided by the f_0 tracking cost $\mathcal{T}_{f_0}$ as a function of the target age τ, required to improve the sensitivity by 10%–50% (from bottom curve to top curve) by switching from f_0 tracking to $(f_0, \dot{f}_0)$ tracking. The f_0 tracking is always faster but less sensitive than $(f_0, \dot{f}_0)$ tracking. For a given percentage of sensitivity improvement, the cost required for choosing $(f_0, \dot{f}_0)$ tracking rather than f_0 tracking increases with τ.

$n = 5$ if the torque is dominated by gravitational radiation reaction, where ϵ is the ellipticity. Integrating the braking law with respect to t, we find that the characteristic spin-down time scale of the signal is given by [33,50]

$$-f_0/\dot{f}_0 = |\xi|^{-1}\tau \qquad (44)$$

with

$$\xi = \frac{1}{n-1}\left[1 - \left(\frac{f_{0\text{birth}}}{f_0}\right)^{1-n}\right]. \qquad (45)$$

The term $(f_{0\text{birth}}/f_0)^{1-n}$ is normally neglected under the assumption $f_0 \ll f_{0\text{birth}}$, yielding $\dot{f}_0 \approx -f_0(n-1)^{-1}\tau^{-1}$ [34,70]. However, this assumption does not necessarily apply to young objects (e.g., $\tau = 0.03$ kyr for SNR 1987A), for which we obtain $|\xi| \lesssim 0.05$ for $f_{0\text{birth}} \lesssim 600$ Hz and $B_0 \lesssim 6 \times 10^{12}$ G with $n = 3$. A detailed discussion can be found in Sec. IIB of Ref. [33].

The indirect upper limit on h_0 derived from energy conservation is given by [3,50,70]

$$h_0 \leq \frac{1}{D}\left(\frac{5GI|\xi|}{2c^3\tau}\right)^{1/2}, \qquad (46)$$

where G is Newton's gravitational constant, c is the speed of light, and D is the distance to the source. The indirect limit on h_0 is lowered because of the second term in (45). On the other hand, the slower spin-down rate $\dot{f}_0 = -f_0|\xi|\tau^{-1}$ benefits HMM tracking by allowing longer T_{drift}.

If we consider a young object with $\tau = 0.03$ kyr as an example, the impact of having $|\xi| = 0.05$ translates into raising T_{drift} by a factor of ≈ 3.

VII. CONCLUSION

In this paper, we describe two practical implementations of an efficient HMM tracker, combined with the maximum likelihood matched filter $\mathcal{F}$ statistic, to economically search for continuous gravitational waves from young neutron stars in SNRs. The HMM incoherently combines the coherent $\mathcal{F}$-statistic outputs from multiple (N_T) data blocks of duration T_{drift}. It tracks rapid, secular spin-down without searching high-order derivatives of the signal frequency. The first implementation, tracking f_0 alone, can simultaneously surmount two challenges in young SNR searches: rapid spin-down and stochastic timing noise. Three scenarios for different spin-down and timing-noise time scales are discussed. Given $T_{\text{obs}} = 83.3$ d, we obtain $h_0^{\text{eff},95\%} \approx 2.4 \times 10^{-26}$ for both weak and strong timing noise in the first two scenarios ($\tau \gtrsim 5$ kyr) and $h_0^{\text{eff},95\%} \approx 8.5 \times 10^{-26}$ in the last scenario ($\tau \lesssim 0.03$ kyr), with $P_{\text{a}} = 1\%$. We expect that $h_0^{95\%}$ is more conservative than the quoted $h_0^{\text{eff},95\%}$ for unknown $\cos \iota$ based on scaling given by (33). The second implementation, tracking f_0 and $\dot{f}_0$, allows longer T_{drift} and hence improves the sensitivity by a factor of a few. The first implementation is always faster and more robust against timing noise. One can achieve better sensitivity by switching from the first implementation to the second. However, it increases the computing cost by 2 to 3 orders of magnitude, depending on τ.

An optimized $\mathcal{F}$-statistic-based semicoherent Einstein@Home search for Cas A ($f_{0\text{max}} = 1.5$ kHz) in the Advanced LIGO O1 run costs approximately 2.7×10^5 core-day, yielding 90% confidence strain upper limit 1.4×10^{-25} [71]. Assuming the same parameters, the method discussed in this paper is expected to provide comparable sensitivity but cost $\sim 10^4$ core-day. The advantage of HMM tracking grows in searches for younger targets, e.g., SNR 1987A.

The methods described in this paper can be applied to extending the searches for the SNRs listed in Ref. [36], which are restricted to coherent segments of duration $T_{\text{drift}} \leq 25.3$ d, using the new data from a whole Advanced LIGO observing run. In addition, the recent work by Anderson *et al.* [72] has identified 76 new Galactic SNR candidates, some of which may be promising candidates for gravitational-wave sources, if the SNR associates are confirmed. The f_0 tracker can be applied to search for targets that are poorly modeled, e.g., a long transient postmerger signal from the binary neutron star merger GW170817 [73] with spin-down time scale $\sim 10^2$–10^4 s. Some modifications are needed, e.g., $L_{o_j q_i}$ should be calculated from the power in SFT bins rather than the $\mathcal{F}$ statistic, because the Earth's rotation can be neglected.

To carry out a search using the methods presented in this paper, the following steps need to be completed in preparation. First, the search parameter ranges need to be determined systematically. The f_0 range is normally chosen to equal the band where the estimated strain sensitivity is below the indirect, τ-based limit [see (46)]. General equations (14) and (15) for calculating $\dot{f}_0$ and $\ddot{f}_0$ are given in Sec. II C. Second, search parameter resolutions need to be calculated using the metric described in Appendix B given a desired mismatch. Third, a systematic Monte Carlo simulation is required for each implementation to determine the detection threshold S_{th} given false alarm and false dismissal probabilities.

APPENDIX A: VITERBI ALGORITHM

The principle of optimality [74] demonstrates that in our special case, all subpaths $Q^{*(k)}$ made up of the first k steps in $Q^{*}(O)$ are optimal for $1 \leq k \leq N_T$. In that sense, the classic Viterbi algorithm [43] provides a recursive, computationally efficient solution to computing $Q^{*}(O)$ in a HMM, reducing the number of operations from $N_Q^{N_T+1}$ to $(N_T + 1)N_Q \ln N_Q$ by binary maximization [42]. A full description of the algorithm can be found in Sec. II D of Ref. [48]. At every forward step k ($1 \leq k \leq N_T$) in the recursion, the algorithm eliminates all but N_Q possible state sequences, and stores the N_Q maximum probabilities

$$\delta_{q_i}(t_k) = L_{o(t_k)q_i} \max_{1 \leq j \leq N_Q} [A_{q_i q_j} \delta_{q_j}(t_{k-1})], \quad \text{(A1)}$$

and previous-step states leading to the retained most likely sequence

$$\Phi_{q_i}(t_k) = \arg \max_{1 \leq j \leq N_Q} [A_{q_i q_j} \delta_{q_j}(t_{k-1})]. \quad \text{(A2)}$$

When backtracking, for $0 \leq k \leq N_T - 1$, we reconstruct the optimal Viterbi path according to

$$q^{*}(t_k) = \Phi_{q^{*}(t_{k+1})}(t_{k+1}). \quad \text{(A3)}$$

APPENDIX B: PHASE METRIC AND COMPUTING COST

The costs of computing the $\mathcal{F}$ statistic (i.e., $L_{o_j q_i}$) and recursively maximizing $P(Q|O)$ depend on the template spacing. We start by discussing the template spacing and cost for a general $\mathcal{F}$-statistic search. To optimize the template spacing, a phase metric is defined. It expresses the signal-to-noise ratio as a function of template spacing along each parameter axis (e.g., f_0, $\dot{f}_0$, $\ddot{f}_0$, …). The mismatch m is defined as the fractional reduction of $\mathcal{F}$-statistic power caused by discrete parameter sampling, with [75–77]

$$m = \sum_{i,j} g_{ij}\Delta\lambda^i\Delta\lambda^j, \tag{B1}$$

$$g_{ij} = \frac{4\pi^2(i+1)(j+1)T_{\text{drift}}^{i+j+2}}{(i+2)!(j+2)!(i+j+3)}. \tag{B2}$$

The indices i and j take integer values from 0 to k, where k indicates the highest-order frequency derivative considered (e.g., $k=2$ for searching up to $\ddot{f}_0$), and $\Delta\lambda^i$ denotes the offset between the true value and the closest template of the ith parameter. For example, the maximum value of $\Delta\lambda^0$ is half the frequency bin width Δf_0, because the signal frequency falls halfway between two templates in the worst case. We choose to adopt $m \leq 0.2$ in line with the Cas A search in S5 data [34] and the SNR searches in S6 data [36]. The highest frequency derivative needed is the largest integer k satisfying $g_{kk}[f_{0\text{max}}^{(k)} - f_{0\text{min}}^{(k)}]^2 > m$ (no summation over k implied), where $f_{0\text{max}}^{(k)}$ and $f_{0\text{min}}^{(k)}$ are the maximum and minimum kth frequency derivatives. In practice, we can choose the bin size of the ith frequency derivative $\Delta f_0^{(i)}$ using the diagonal terms of (B2) to satisfy

$$\sum_{i=0}^{k} g_{ii}[\Delta f_0^{(i)}]^2 < 4m. \tag{B3}$$

Monte Carlo simulations are needed to accurately calculate the required bin sizes for a given m. Taking into consideration the off-diagonal terms of (B2) yields bin sizes close to the empirical Monte Carlo results. A tiling algorithm is described in detail in Ref. [78]. Combining (14), (15), and (B2), the number of templates $\mathcal{N}$ needed for $k=2$ is [50,78]

$$\mathcal{N} = 0.35m^{-3/2}(\det g)^{1/2}f_{0\text{max}}^3\tau^{-3}, \tag{B4}$$

with $f_{0\text{min}} \ll f_{0\text{max}}$ typically.

The computing time of a coherent $\mathcal{F}$-statistic search over one block of duration T_{drift} is given by

$$\mathcal{T} = \kappa\mathcal{N}\beta N_{\text{ifo}}T_{\text{drift}}T_{\text{SFT}}^{-1}, \tag{B5}$$

where κ is the time to compute the $\mathcal{F}$ statistic per template per SFT,[7] N_{ifo} is the number of interferometers, and β is the percentage of time that the interferometers collect data (i.e., duty cycle). For most of the young targets discussed in Ref. [36], $\ddot{f}_0$ is normally small. Only a few $\ddot{f}_0$ values need to be searched. For example, we obtain $\ddot{f}_0 \lesssim 1 \times 10^{-18}$ Hz s^{-2} from (14) and (15) for $\tau \gtrsim 1$ kyr and $f_0 \lesssim 600$ Hz and $\Delta\ddot{f}_0 \sim 10^{-18}$ Hz s^{-2} from (B2) and (B3) with $T_{\text{drift}} = 10$ d. In this example, only one value of $\ddot{f}_0$ is searched and the cost scaling in Eq. (B5) reduces to $f_{0\text{max}}^2\tau^{-1}T_{\text{drift}}^4$.[8] If we assume that, only one value of $\ddot{f}_0$ is searched. For $\kappa = 4 \times 10^{-8}$ s, $m = 0.2$, $\beta = 1$, $N_{\text{ifo}} = 2$, $T_{\text{SFT}} = 1800$ s, and $N_{\text{core}} = 10^3$ cores running in parallel, we obtain

$$\mathcal{T}_{f_0,\dot{f}_0} = 0.36 \text{ d}\left(\frac{f_{0\text{max}}}{0.6 \text{ kHz}}\right)^2\left(\frac{0.3 \text{ kyr}}{\tau}\right)\left(\frac{T_{\text{drift}}}{10 \text{ d}}\right)^4\left(\frac{10^3}{N_{\text{core}}}\right). \tag{B6}$$

However, for very young objects (e.g., $\tau \lesssim 0.03$ kyr) with larger $\ddot{f}_0$, the cost scales as $\mathcal{T}_{f_0,\dot{f}_0,\ddot{f}_0} \propto f_{0\text{max}}^3\tau^{-3}T_{\text{drift}}^7$.

Figure 10 shows the cost of computing the $\mathcal{F}$ statistic over a coherent segment T_{drift} (in units of core-day). For concreteness, we fix $f_{0\text{max}} = 600$ Hz. In a real search, $f_{0\text{max}}$ is a function of τ, because we determine $f_{0\text{max}}$ to be the maximum frequency where the estimated strain sensitivity of the search beats the indirect spin-down limit [see Eq. (46)]. If we compute $\mathcal{F}(f_0,\dot{f}_0)$ (or search a single $\ddot{f}_0$ value), the costs for objects with $\tau = 0.3$ kyr and 1 kyr are indicated by the two solid curves. A coherent $\mathcal{F}$-statistic search or a stack-slide-based semicoherent $\mathcal{F}$-statistic search requires searching higher-order derivatives for objects with $\tau \lesssim 0.3$ kyr. The two dashed curves (top and bottom) represent the cost of computing $\mathcal{F}(f_0,\dot{f}_0,\ddot{f}_0)$ for objects with $\tau = 0.03$ kyr and 0.1 kyr, respectively.

The serial clock time for computing can be reduced by parallelization. For 10^3 nodes running in parallel, a coherent $\mathcal{F}$-statistic search over $T_{\text{drift}} = 10$ d takes about 9 h for an object with $\tau = 0.3$ kyr (e.g., Cas A), and about 10 d for an object with $\tau = 0.1$ kyr (e.g., G1.9 + 0.3). In reality, the cost indicated by the top dashed curve for an object with $\tau = 0.03$ kyr (e.g., SNR 1987A) is still underestimated, because $\dddot{f}_0$ and higher-order derivatives must be searched using a stack-slide-based semicoherent method.

---

[7]The value of κ depends on T_{SFT} and the CPU architecture. An example in Sec. 5 of Ref. [50] quotes $\kappa = 6 \times 10^{-7}$ s ($T_{\text{SFT}} = 1800$ s) on Australian Partnership for Advanced Computing (APAC) resources. We adopt a more recent estimate, $\kappa = 4 \times 10^{-8}$ s, in this paper.

[8]It is shown in Ref. [36] that in the S6 search the computing cost scales approximately as $f_{0\text{max}}^{2.2}\tau^{-1.1}T_{\text{drift}}^4$.
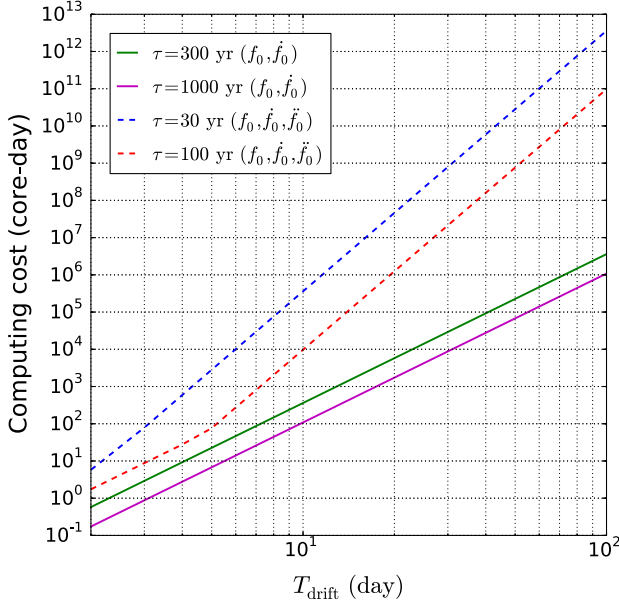
FIG. 10.   Computing cost (in core-days) of a coherent $\mathcal{F}$-statistic search with $T_{\mathrm{obs}} = T_{\mathrm{drift}}$ as a function of T_{drift} (in days). The two solid curves (top and bottom) represent computing $\mathcal{F}(f_0, \dot{f}_0)$ (or include a single $\ddot{f}_0$ value) for objects with $\tau = 0.3$ kyr and 1 kyr, respectively. The two dashed curves (top and bottom) represent computing $\mathcal{F}(f_0, \dot{f}_0, \ddot{f}_0)$ for objects with $\tau = 0.03$ kyr and 0.1 kyr, respectively. Parameters: $f_{0\mathrm{max}} = 600$ Hz.

We do not search second- or higher-order derivatives of the frequency in the HMM tracking. We start by discussing the $(f_0, \dot{f}_0)$ tracking. In the two-dimensional tracking, we can always substitute the maximum $\ddot{f}_0$ in the range (15) into (34) to choose T_{drift} and ignore $\ddot{f}_0$ (or search a single value). However, for very young objects (e.g., $\tau \lesssim 0.03$ kyr) with larger $\ddot{f}_0$, there can be sensitivity loss due to the short T_{drift} derived from (34). The relation between theoretical sensitivity and T_{drift} is discussed in Appendix E. The estimate of $\mathcal{T}$ in (B6) stands for the time required to calculate the $\mathcal{F}$ statistic over one block of coherent segment T_{drift}. For HMM tracking, we need to add up the time required to calculate all the required values of $\mathcal{F}(f_0, \dot{f}_0)$. In addition, there is a second component to the computing cost, namely solving the HMM. HMM tracking incoherently combines the $\mathcal{F}$-statistic outputs from $N_T = T_{\mathrm{obs}}/T_{\mathrm{drift}}$ blocks of data. The Viterbi algorithm computes $Q^*(O)$ via $(N_T + 1)N_Q \ln N_Q$ operations [48]. The total computing cost is dominated by the cost of computing N_T blocks of the $\mathcal{F}$ statistic, scaling as $\mathcal{T} \propto N_T f_{0\mathrm{max}}^2 \tau^{-1} T_{\mathrm{drift}}^4$. If we take $T_{\mathrm{drift}} = 5$ d as an example, Fig. 11 shows the computing cost of a semicoherent HMM search (in units of core-day) as a function of $T_{\mathrm{obs}} = N_T T_{\mathrm{drift}}$ for targets with $\tau = 0.03$ kyr, 0.1 kyr, 0.3 kyr, and 1 kyr, respectively. In practice, $T_{\mathrm{drift}} > 5$ d is allowed for older targets and $T_{\mathrm{drift}} < 5$ d is required for younger ones.
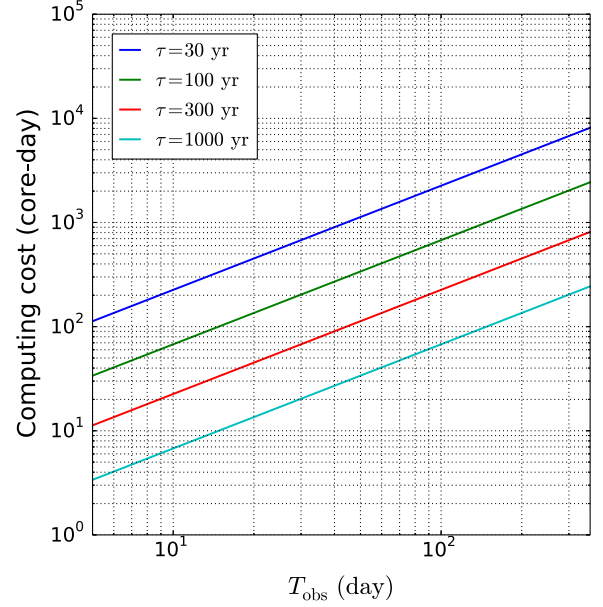

FIG. 11.   Computing cost (in core-days) of a semicoherent HMM search as a function of T_{obs} (in days) with T_{drift} fixed. The four curves (from top to bottom) represent objects with $\tau = 0.03$ kyr, 0.1 kyr, 0.3 kyr, and 1 kyr, respectively. Parameters: $f_{0\mathrm{max}} = 600$ Hz, $T_{\mathrm{drift}} = 5$ d, $N_T = T_{\mathrm{obs}}/T_{\mathrm{drift}}$.

When tracking f_0 alone, the search is always cheaper. We choose $\Delta f_0 = 1/(2T_{\mathrm{drift}})$, satisfying $m \leq 0.2$. The metric given by (B2) is no longer needed for $k = 0$. Hence the number of templates and cost needed for computing the $\mathcal{F}$-statistic over each block of T_{drift} in (B4) and (B5) reduces to

$$\mathcal{N} = 2T_{\mathrm{drift}} f_{0\mathrm{max}}, \tag{B7}$$

and

$$\mathcal{T}_{f_0} = 2\kappa\beta N_{\mathrm{ifo}} T_{\mathrm{drift}}^2 T_{\mathrm{SFT}}^{-1} f_{0\mathrm{max}}. \tag{B8}$$

The total cost scales $\propto N_T f_{0\mathrm{max}} T_{\mathrm{drift}}^2$ when tracking f_0 alone, saving a factor $\sim f_{0\mathrm{max}} T_{\mathrm{drift}}^2$ compared to the $(f_0, \dot{f}_0)$ tracking.

APPENDIX C: T_{drift} GIVEN τ

We assume purely electromagnetic spin-down ($\dot{f}_0 \propto B_0^2 f_0^n$, $n = 3$) for simplicity, which gives

$$\dot{f}_0(t) = -\eta f_0(t)^3, \tag{C1}$$

where the coefficient $\eta \propto B_0^2$ is a positive constant. At time $t = 0$ when the star was born, we have $f_0(t) = f_{0\mathrm{birth}}$. The differential equation (C1) has the solution

$$1 - \left(\frac{f_0}{f_{0\text{birth}}}\right)^2 = -\frac{2\tau\dot{f}_0}{f_0}. \tag{C2}$$

Substituting $\dot{f}_0 = -(2T_{\text{drift}}^2)^{-1}$ from (26) into (C2), we obtain

$$T_{\text{drift}} = \tau^{1/2}f_0^{-1/2}\left[1 - \left(\frac{f_0}{f_{0\text{birth}}}\right)^2\right]^{-1/2}. \tag{C3}$$

APPENDIX D: TRANSITION PROBABILITY MATRIX FOR $f_0, \dot{f}_0$ TRACKING

We first derive the transition probabilities corresponding to the substate $\dot{f}_0$. Using Eqs. (14) and (15), the range of $\ddot{f}_0$ is given by

$$\frac{0.2f_{0\text{min}}}{\tau^2} \lesssim \ddot{f}_0 \lesssim \frac{2f_{0\text{max}}}{\tau^2}, \tag{D1}$$

where $f_{0\text{min}}$ and $f_{0\text{max}}$ are the minimum and maximum f_0 being searched. The maximum $\ddot{f}_0$ is more than 2 orders of magnitude larger than the minimum $\ddot{f}_0$. We assume that $\ddot{f}_0$ is uniformly distributed in the range $0 \leq \ddot{f}_0 \leq \ddot{f}_{0\text{max}}$. At each step, given Eq. (34), $\dot{f}_0$ jumps at most one bin up or stays in the same bin with equal probability 1/2.

We then estimate the number of bins f_0 moves during each step. Equation (35) is more precisely given by

$$f_0(t_{\text{n}}) + \dot{f}_0(t_{\text{n}})T_{\text{drift}} \leq f_0(t_{\text{n+1}})$$
$$\leq f_0(t_{\text{n}}) + [\dot{f}_0(t_{\text{n}}) + \Delta\dot{f}_0]T_{\text{drift}}. \tag{D2}$$

Let us write $q(t_{\text{n}}) = [f_0(t_{\text{n}}), \dot{f}_0(t_{\text{n}})] = q_{ij}$, where i and j index f_0 and $\dot{f}_0$ bins, respectively. Then the number of bins that f_0 moves from step t_{n} to step $t_{\text{n+1}}$, denoted by Δi, takes the minimum and maximum values

$$\Delta i_{\text{min}}(j) = \text{floor}(|\dot{f}_{0j+1}|T_{\text{drift}}/\Delta f_0), \tag{D3}$$

$$\Delta i_{\text{max}}(j) = \text{ceil}(|\dot{f}_{0j}|T_{\text{drift}}/\Delta f_0), \tag{D4}$$

where floor(x) denotes the largest integer smaller than or equal to x, ceil(x) denotes the smallest integer larger than or equal to x, and $\dot{f}_{0j}$ is the value of $\dot{f}_0$ in the jth $\dot{f}_0$ bin. In other words, $f_0(t_{\text{n+1}})$ can be located in any bin within the range $[i - \Delta i_{\text{max}}, i - \Delta i_{\text{min}}]$ with uniform probability.[9] The two-dimensional transition probability matrix is given by

$$A_{q_{i-\Delta i, j+1}q_{ij}} = A_{q_{i-\Delta i, j}q_{ij}} \tag{D5}$$

$$= \{2[\Delta i_{\text{max}}(j) - \Delta i_{\text{min}}(j) + 1]\}^{-1}, \tag{D6}$$

---

[9]Since $\dot{f}_0$ is negative, we always have $f_0(t_{\text{n+1}}) \leq f_0(t_{\text{n}})$.

where Δi takes integer values $\Delta i_{\text{min}}(j) \leq \Delta i \leq \Delta i_{\text{max}}(j)$, and all other terms are zero.

APPENDIX E: ANALYTIC SENSITIVITY SCALINGS

In this section, we present an approximate analytic formula for the search sensitivity, based on a few general assumptions. Deviations are discussed in detail in Refs. [68,69]. Accurate sensitivity scalings require Monte Carlo simulations for each implementation of the search, as shown in Sec. IV.

The sensitivity of a search can be defined in terms of the characteristic gravitational-wave strain corresponding to 95% detection efficiency. For a coherent $\mathcal{F}$-statistic search over one block of T_{drift}, searching up to the highest frequency derivative required for a given mismatch, it takes the form [36,50]

$$h_0^{95\%}(f) = \Theta S_h(f)^{1/2}(\beta T_{\text{drift}})^{-1/2}, \tag{E1}$$

where Θ is a statistical threshold, depending on the shape of the parameter space manifold. One finds $30 \lesssim \Theta \lesssim 40$ for a directed search of the type discussed in this paper [50]. The term βT_{drift} gives the length of the interferometer data in the time span T_{drift}.

As every block of $\mathcal{F}$-statistic output over T_{drift} is chi-squared distributed with 4 degrees of freedom,[10] and the chi-squared distribution is additive, we can calculate the PDF of $z = \ln P(Q|O)$ along the true signal path from (11) and (13) by multiplying both the degrees of freedom and the non-centrality parameter by $N_T = T_{\text{obs}}/T_{\text{drift}}$. If $Q^*(O)$ coincides exactly with the true path, we obtain

$$p(z) = \chi^2\left[z; \frac{4T_{\text{obs}}}{T_{\text{drift}}}, \frac{Kh_0^2 T_{\text{obs}}}{S_h(f)}\right]. \tag{E2}$$

If $Q^*(O)$ does not intersect the true path anywhere, we have

$$p(z) = \chi^2\left(z; \frac{4T_{\text{obs}}}{T_{\text{drift}}}, 0\right). \tag{E3}$$

Combining (E2) and (E3), the signal-to-noise ratio after N_T steps of the HMM equals ρ_0', given by

$$\rho_0'^2 = \frac{\mu_{\text{signal}} - \mu_{\text{noise}}}{\sigma_{\text{noise}}} \tag{E4}$$

---

[10]Here we assume that the $\mathcal{F}$ statistic is independently and identically distributed. The estimate requires modification when applied to real interferometer data, where the noise is nonstationary and/or non-Gaussian. A more robust Bayesian framework is introduced in Ref. [79] to analyze the $\mathcal{F}$ statistic in the presence of instrumental artifacts.
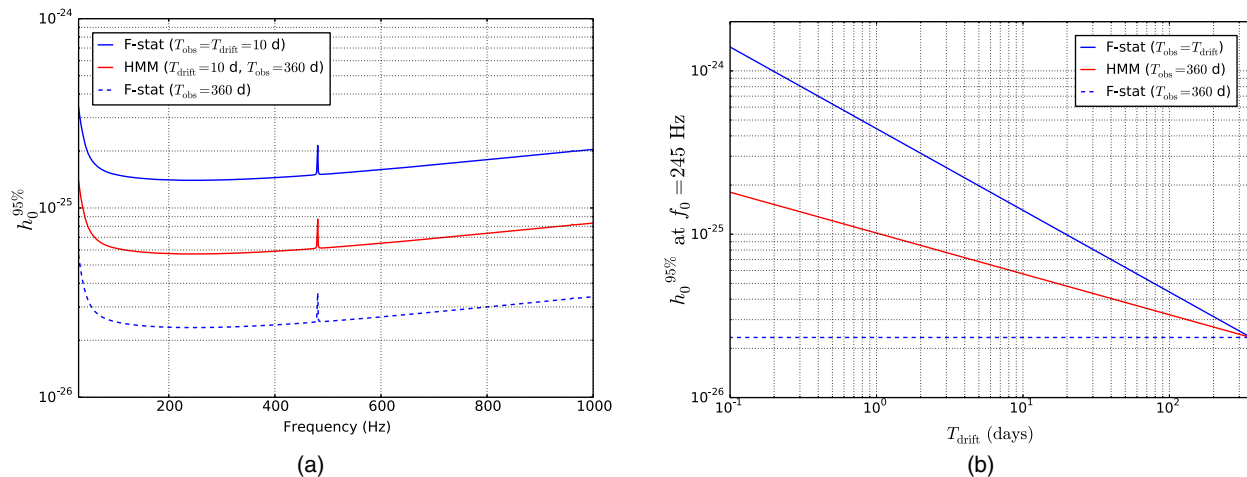
FIG. 12. Analytical sensitivity $h_0^{95\%}$ of two coherent $\mathcal{F}$-statistic searches (blue curves) and a semicoherent HMM search (red curve) for an isolated young neutron star at the design sensitivity of Advanced LIGO. The blue solid curve indicates a coherent $\mathcal{F}$-statistic search of duration T_{drift}, the maximum practical duration set by spin-down in Ref. [36]. The blue dashed curve indicates a coherent $\mathcal{F}$-statistic search with $T_{\text{obs}} = 360$ d. The red curve indicates a HMM search with $T_{\text{obs}} = 360$ d and $N_T = T_{\text{obs}}/T_{\text{drift}}$. (a) $h_0^{95\%}$ as a function of signal frequency f_0. (b) Minimum $h_0^{95\%}$ [i.e., $h_0^{95\%}$ achieved at 245 Hz in (a)] as a function of T_{drift}. The HMM sensitivity scales as $\sim T_{\text{drift}}^{-1/4}$ for fixed T_{obs}. When T_{drift} is fixed, the HMM (red curve) improves upon the $\mathcal{F}$-statistic search (blue solid curve) by a factor of $\sim N_T^{1/4}$. The spikes in the first panel are instrumental lines predicted to occur in Advanced LIGO at its design sensitivity. (Statistical threshold: $\Theta = 35$.)

$$\propto \frac{h_0^2}{S_h(f)} (T_{\text{obs}} T_{\text{drift}})^{1/2}, \tag{E5}$$

where $\mu_{\text{signal}} = N_T \rho_0^2$ and $\mu_{\text{noise}} = 0$ are the noncentralities of the distributions in (E2) and (E3), respectively, and $\sigma_{\text{noise}} = (8N_T)^{1/2}$ is the standard deviation of the distribution in (E3). Hence we obtain

$$h_0^{95\%}(f) = \Theta S_h(f)^{1/2} (T_{\text{obs}} T_{\text{drift}})^{-1/4}, \tag{E6}$$

assuming $\beta = 1$. When $T_{\text{obs}} = T_{\text{drift}}$, Eq. (E6) reduces to (E1).

By way of illustration, we compute $h_0^{95\%}$ for HMM tracking with $T_{\text{obs}} = N_T T_{\text{drift}} = 360$ d and compare the result with a coherent $\mathcal{F}$-statistic search limited to $T_{\text{obs}} = T_{\text{drift}}$ as in Ref. [36]. We take $\Theta = 35$ and let $S_h(f)$ be the Advanced LIGO design noise PSD in (E1). Figure 12 shows the results. The blue solid curve, red solid curve, and blue dashed curve indicate an $\mathcal{F}$-statistic search of duration T_{drift}, a HMM search of duration $N_T T_{\text{drift}}$, and a fully coherent $\mathcal{F}$-statistic search with $T_{\text{obs}} = 360$ d, respectively.

Figure 12(a) plots $h_0^{95\%}$ as a function of signal frequency. When T_{drift} is fixed [e.g., $T_{\text{drift}} = 10$ d in Fig. 12(a)], the HMM tracking of duration $N_T T_{\text{drift}}$ improves upon the sensitivity of the $\mathcal{F}$-statistic search of duration T_{drift} by a factor of $\sim N_T^{1/4}$. Figure 12(b) plots the minimum $h_0^{95\%}$ in Fig. 12(a) achieved in the band where the detectors are most sensitive (at 245 Hz) as a function of T_{drift}. The sensitivity achievable by the HMM scales as $\sim T_{\text{drift}}^{-1/4}$ for fixed $T_{\text{obs}} = 1$ yr. Figures 12(a) and 12(b) demonstrate together the scaling indicated by (E6). A fully coherent search using all the data (duration $N_T T_{\text{drift}}$) indicated by the blue dashed curve is more sensitive than the HMM of course. However, it is computationally expensive.[11] The theoretical scalings here also apply approximately to other $\mathcal{F}$-statistic-based semicoherent searches.

---

[11]One fully coherent search directed at the isolated compact object Calvera has been carried out, using Initial LIGO S5 data ($T_{\text{obs}} = 2$ yr). It is based on a resampling technique and saves computing cost by a factor $T_{\text{obs}}(\log T_{\text{obs}})^{-1}$, yielding a minimum upper limit $h_0^{95\%} = 1.14 \times 10^{-25}$ at 152 Hz [80].

[1] B. Abbott *et al.*, Phys. Rev. D **76**, 082001 (2007).

[2] LIGO Scientific Collaboration and Virgo Collaboration, arXiv:1203.2674.

[3] K. Riles, Prog. Part. Nucl. Phys. **68**, 1 (2013).

[4] G. Ushomirsky, C. Cutler, and L. Bildsten, Mon. Not. R. Astron. Soc. **319**, 902 (2000).

[5] N. K. Johnson-McDaniel and B. J. Owen, Phys. Rev. D **88,** 044004 (2013).

[6] C. Cutler, Phys. Rev. D **66,** 084025 (2002).

[7] A. Mastrano, A. Melatos, A. Reisenegger, and T. Akgün, Mon. Not. R. Astron. Soc. **417,** 2288 (2011).

[8] P. D. Lasky and A. Melatos, Phys. Rev. D **88,** 103005 (2013).

[9] B. J. Owen, L. Lindblom, C. Cutler, B. F. Schutz, A. Vecchio, and N. Andersson, Phys. Rev. D **58,** 084020 (1998).

[10] J. S. Heyl, Astrophys. J. **574,** L57 (2002).

[11] P. Arras, E. E. Flanagan, S. M. Morsink, A. K. Schenk, S. A. Teukolsky, and I. Wasserman, Astrophys. J. **591,** 1129 (2003).

[12] R. Bondarescu, S. A. Teukolsky, and I. Wasserman, Phys. Rev. D **79,** 104003 (2009).

[13] C. Peralta, A. Melatos, M. Giacobello, and A. Ooi, Astrophys. J. **644,** L53 (2006).

[14] C. A. van Eysden and A. Melatos, Classical Quantum Gravity **25,** 225020 (2008).

[15] M. F. Bennett, C. A. Van Eysden, and A. Melatos, Mon. Not. R. Astron. Soc. **409,** 1705 (2010).

[16] A. Melatos, J. A. Douglass, and T. P. Simula, Astrophys. J. **807,** 132 (2015).

[17] P. Haensel, V. A. Urpin, and D. G. Iakovlev, Astron. Astrophys. **229,** 133 (1990).

[18] O. Y. Gnedin, D. G. Yakovlev, and A. Y. Potekhin, Mon. Not. R. Astron. Soc. **324,** 725 (2001).

[19] B. Knispel and B. Allen, Phys. Rev. D **78,** 044031 (2008).

[20] A. Melatos and C. Peralta, Astrophys. J. **709,** 77 (2010).

[21] A. Melatos, Astrophys. J. **761,** 32 (2012).

[22] J. McKenna and A. G. Lyne, Nature (London) **343,** 349 (1990).

[23] S. L. Shemar and A. G. Lyne, Mon. Not. R. Astron. Soc. **282,** 677 (1996).

[24] J. O. Urama and P. N. Okeke, Mon. Not. R. Astron. Soc. **310,** 313 (1999).

[25] A. Melatos, C. Peralta, and J. S. B. Wyithe, Astrophys. J. **672,** 1103 (2008).

[26] A. Mastrano and A. Melatos, Mon. Not. R. Astron. Soc. **361,** 927 (2005).

[27] A. Melatos and C. Peralta, Astrophys. J. **662,** L99 (2007).

[28] K. Glampedakis and N. Andersson, Phys. Rev. Lett. **102,** 141101 (2009).

[29] J. Middleditch, F. E. Marshall, Q. D. Wang, E. V. Gotthelf, and W. Zhang, Astrophys. J. **652,** 1531 (2006).

[30] B. Abbott et al. (LIGO Scientific Collaboration), Rep. Prog. Phys. **72,** 076901 (2009).

[31] J. Abadie et al., Phys. Rev. Lett. **107,** 271102 (2011).

[32] C. Messenger, LIGO Document No. T1000195, 2011.

[33] L. Sun, A. Melatos, P. D. Lasky, C. T. Y. Chung, and N. S. Darman, Phys. Rev. D **94,** 082004 (2016).

[34] J. Abadie et al., Astrophys. J. **722,** 1504 (2010).

[35] S. J. Zhu, M. A. Papa, H.-B. Eggenstein, R. Prix, K. Wette, B. Allen, O. Bock, D. Keitel, B. Krishnan, B. Machenschalk, M. Shaltev, and X. Siemens, Phys. Rev. D **94,** 082008 (2016).

[36] J. Aasi et al., Astrophys. J. **813,** 39 (2015).

[37] B. Abbott et al., Phys. Rev. Lett. **116,** 131103 (2016).

[38] G. Mendell and M. Landry, LIGO Technical Document No. LIGO-T050003, 2005.

[39] V. Dergachev, LIGO Technical Document LIGO-T050186, 2005.

[40] S. Dhurandhar, B. Krishnan, H. Mukhopadhyay, and J. T. Whelan, Phys. Rev. D **77,** 082001 (2008).

[41] P. R. Brady and T. Creighton, Phys. Rev. D **61,** 082001 (2000).

[42] B. G. Quinn and E. J. Hannan, The Estimation and Tracking of Frequency (Cambridge University Press, Cambridge, 2001), p. 266.

[43] A. Viterbi, IEEE Trans. Inf. Theory **13,** 260 (1967).

[44] B. P. Abbott et al., Phys. Rev. D **95,** 122003 (2017).

[45] P. Jaranowski, A. Królak, and B. F. Schutz, Phys. Rev. D **58,** 063001 (1998).

[46] C. Van Den Broeck, Classical Quantum Gravity **22,** 1825 (2005).

[47] R. Prix, Phys. Rev. D **75,** 023004 (2007).

[48] S. Suvorova, L. Sun, A. Melatos, W. Moran, and R. J. Evans, Phys. Rev. D **93,** 123009 (2016).

[49] R. Prix, LIGO Report No. T0900149, 2011.

[50] K. Wette et al., Classical Quantum Gravity **25,** 235011 (2008).

[51] N. Andersson, D. Antonopoulou, C. M. Espinoza, B. Haskell, and W. C. G. Ho, arXiv:1711.05550.

[52] G. Hobbs, A. G. Lyne, and M. Kramer, Mon. Not. R. Astron. Soc. **402,** 1027 (2010).

[53] R. M. Shannon and J. M. Cordes, Astrophys. J. **725,** 1607 (2010).

[54] G. Ashton, D. I. Jones, and R. Prix, Phys. Rev. D **91,** 062009 (2015).

[55] J. M. Cordes and D. J. Helfand, Astrophys. J. **239,** 640 (1980).

[56] S. Price, B. Link, S. N. Shore, and D. J. Nice, Mon. Not. R. Astron. Soc. **426,** 2507 (2012).

[57] A. Lyne, G. Hobbs, M. Kramer, I. Stairs, and B. Stappers, Science **329,** 408 (2010).

[58] M. A. Alpar, R. Nandkumar, and D. Pines, Astrophys. J. **311,** 197 (1986).

[59] P. Jones, Mon. Not. R. Astron. Soc. **246,** 364 (1990).

[60] A. Melatos and B. Link, Mon. Not. R. Astron. Soc. **437,** 21 (2014).

[61] J. M. Cordes and G. S. Downs, Astrophys. J. Suppl. Ser. **59,** 343 (1985).

[62] G. H. Janssen and B. W. Stappers, Astron. Astrophys. **457,** 611 (2006).

[63] K. S. Cheng, Astrophys. J. **321,** 799 (1987).

[64] K. S. Cheng, Astrophys. J. **321,** 805 (1987).

[65] J. O. Urama, B. Link, and J. M. Weisberg, Mon. Not. R. Astron. Soc. Lett. **370,** L76 (2006).

[66] D. H. Shoemaker et al., LIGO Report No. T0900288, 2009.

[67] C. Messenger, H. J. Bulten, S. G. Crowder, V. Dergachev, D. K. Galloway, E. Goetz, R. J. G. Jonker, P. D. Lasky, G. D. Meadors, A. Melatos, S. Premachandra, K. Riles, L. Sammut, E. H. Thrane, J. T. Whelan, and Y. Zhang, Phys. Rev. D **92,** 023006 (2015).

[68] K. Wette, Phys. Rev. D **85,** 042003 (2012).

[69] R. Prix and M. Shaltev, Phys. Rev. D **85,** 084010 (2012).

[70] C. T. Y. Chung, A. Melatos, B. Krishnan, and J. T. Whelan, Mon. Not. R. Astron. Soc. **414,** 2650 (2011).

[71] J. Ming, M. A. Papa, B. Krishnan, R. Prix, C. Beer, S. J. Zhu, H.-B. Eggenstein, O. Bock, and B. Machenschalk, Phys. Rev. D **97**, 024051 (2018).

[72] L. D. Anderson, Y. Wang, S. Bihr, H. Beuther, F. Bigiel, E. Churchwell, S. C. O. Glover, A. A. Goodman, T. Henning, M. Heyer, R. S. Klessen, H. Linz, S. N. Longmore, K. M. Menten, J. Ott, N. Roy, M. Rugel, J. D. Soler, J. M. Stil, and J. S. Urquhart, Astron. Astrophys. **605**, A58 (2017).

[73] B. P. Abbott *et al.*, Astrophys. J. **851**, L16 (2017).

[74] R. Bellman, (Princeton University Press, Princeton, 1957), Vol. 70, p. 342.

[75] P. R. Brady, T. Creighton, C. Cutler, and B. F. Schutz, Phys. Rev. D **57**, 2101 (1998).

[76] B. J. Owen, Phys. Rev. D **53**, 6749 (1996).

[77] D. M. Whitbeck, Ph.D. thesis, The Pennsylvania State University, 2006.

[78] R. Prix, Classical Quantum Gravity **24**, S481 (2007).

[79] D. Keitel, R. Prix, M. A. Papa, P. Leaci, and M. Siddiqi, Phys. Rev. D **89**, 064023 (2014).

[80] P. K. Patel, Ph.D. thesis, California Institute of Technology, 2011.

Correction: The third time derivative of frequency $\dddot{f}_0$ was rendered improperly during the conversion process five times and has been fixed.